

PhenomXPNR: An improved gravitational wave model linking precessing inspirals and NR-calibrated merger-ringdown

Eleanor Hamilton,¹ Marta Colleoni,¹ Jonathan E. Thompson,^{2,3} Charlie Hoy,⁴
 Anna Heffernan,¹ Meryl Kinnear,⁵ Jorge Valencia,¹ Felip A. Ramis Vidal,¹ Cecilio
 García-Quirós,⁶ Shrobona Ghosh,^{7,8} Lionel London,⁹ Mark Hannam,⁵ and Sascha Husa^{10,1}

¹*Departament de Física, Universitat de les Illes Balears, IAC3 – IEEC, Crta. Valldemossa km 7.5, E-07122 Palma, Spain*

²*Mathematical Sciences & STAG Research Centre, University of Southampton, Southampton, SO17 1BJ, United Kingdom*

³*Theoretical Astrophysics Group, California Institute of Technology, Pasadena, CA 91125, U.S.A.*

⁴*Institute of Cosmology & Gravitation, University of Portsmouth, Portsmouth, United Kingdom*

⁵*Gravity Exploration Institute, School of Physics and Astronomy, Cardiff University, Cardiff CF24 3AA, United Kingdom*

⁶*Physik-Institut, Universität Zürich, Winterthurerstrasse 190, 8057 Zürich, Switzerland*

⁷*Max Planck Institute for Gravitational Physics (Albert Einstein Institute), Callinstrasse 38, D-30167 Hannover, Germany*

⁸*Leibniz University Hannover, 30167 Hannover, Germany*

⁹*King's College London, Strand, London WC2R 2LS, United Kingdom*

¹⁰*Institut de Ciències de l'Espai (ICE, CSIC), Campus UAB, Carrer de Can Magrans s/n, 08193 Cerdanyola del Vallès, Spain*

(Dated: July 4, 2025)

We present the frequency-domain quasi-circular precessing binary-black-hole model PHENOMXPNR. This model combines the most precise available post-Newtonian description of the evolution of the precession dynamics through inspiral with merger-ringdown model informed by numerical relativity. This, along with a phenomenological model of the dominant multipole asymmetries, results in the most accurate and complete representation of the physics of precessing binaries natively in the frequency-domain to date. All state-of-the-art precessing models show bias when inferring binary parameters in certain regions of the parameter space. We demonstrate that the developments presented ensure that for some precessing systems PHENOMXPNR shows the least degree of bias. Further, as a phenomenological, frequency-domain model, PHENOMXPNR remains one of the most computationally efficient models available and is therefore well-suited to the era of gravitational-wave astronomy with its ever growing rate of detected signals.

I. INTRODUCTION

Since 2015 ~ 100 gravitational wave signals have been detected by the LIGO-Virgo-KAGRA (LVK) network [1], most of them from merging black holes. The black holes' properties are measured by comparing the detector data to theoretical signal models. The measurement accuracy is determined by the statistical error due to detector noise, but also the accuracy of the models themselves. As detector sensitivity increases, so does the required model accuracy. Detector upgrades have led to roughly a factor of two increase in sensitivity over the last decade [2], with a further factor of two for current generation ground-based detectors projected into the 2030s, and another order of magnitude improvement expected in next-generation ground-based detectors by 2040 [3–6]. In parallel, successive improvements in waveform models have seen improved tuning to analytic approximations and numerical relativity (NR) simulations, and inclusion of more detailed physical effects.

In this paper, we focus on the modelling of spin precession effects [7, 8]. This is challenging due to the complex phenomenology and high dimensionality of such systems. There is a high computational cost required to densely cover the seven-dimensional parameter space (mass ratio and two spin vectors) with long NR simulations in order to understand their detailed characteristics. Waveform models that describe precessing spins have however already been used to analyse gravitational wave signals since the first gravitational wave detection [9, 10]. This has been made possible by the twisting-up approximation [11–14], which provides an approximate map between precessing and non-precessing waveforms. Many precessing gravitational wave models [15–19] utilise information from post-Newtonian (PN) and black-hole (BH) perturbation theory to describe this mapping for the entire inspiral-merger-ringdown (IMR) signal without employing information from

NR in order to ensure an accurate merger-ringdown prescription.

Increasing detector sensitivity results in an increased observable volume of the universe and a consequent increase in the number of detections. Analysing the large number of detected signals anticipated in this era of gravitational wave astronomy requires both highly accurate and highly computationally efficient models. To date, state-of-the-art models have used three main modelling approaches: phenomenological waveform (Phenom) models [15–17, 20–22], the effective-one-body (EOB) paradigm [18, 19, 23–26] and surrogate models [27–29]. The Phenom and EOBNR models use semi-analytic approximations to describe the gravitational wave signal during the black holes' inspiral and NR simulations to inform a model of the merger and ringdown. The surrogate models are trained purely on NR or hybrid waveforms to accurately model the signal, without analytic approximations over the binary parameter space of the training data.

The above models can be further divided into two broad categories; those where the modelling takes place natively in the time domain, and those where it occurs in the frequency domain. Fast frequency-domain (FD) models constructed in the Phenom approach, such as the model presented here, are typically more convenient for analysis of detected gravitational wave signals from compact binary sources. The analysis of a single gravitational wave signal requires millions of likelihood evaluations: under the assumption of stationary and Gaussian noise, the noise covariance matrix of GW detectors becomes diagonal in the Fourier domain and the likelihood can be recast into a computationally efficient form known as the Whittle likelihood [30]. This assumption, combined with the circulant hypothesis, enables the use of classical sampling methods to perform Bayesian parameter estimation in the FD, and facilitates the marginalisation of the likelihood over nuisance

parameters [31].

The PhenomX family of models [15, 16, 20–22] constitutes the current generation of FD models for the gravitational wave signal from coalescing binaries. These have been used e.g. in the GWTC-3 catalog of LVK observations [32]. The underlying aligned-spin models (PHENOMXAS [15] for the dominant quadrupole modes, which is extended to other spherical harmonics in PHENOMXHM [20]) are calibrated to NR simulations of non-precessing (aligned-spin) binaries up to mass ratios of 1:18, and black-hole spins up to 0.995 in the equal mass limit and up to 0.85 at higher mass ratios, with input from PN and EOB results for the inspiral, and perturbation-theory results to inform the ringdown and the extreme-mass-ratio limit. In the PHENOMXO4A [22] extension of these models, spin-precession effects are captured during the inspiral by a multi-scale analysis (MSA) model [33, 34], and through the merger and ringdown are tuned to single-spin NR simulations up to mass ratios of 1:8 and spins up to 0.8 [35]. PHENOMXO4A also includes a model of the dominant contribution to the multipole asymmetry that leads to out-of-plane recoil of the remnant black hole [36]. In the PHENOMXPHM-SPINTAYLOR [16] model there is no NR tuning of merger-ringdown precession effects, but the inspiral spin precession is described by evolving the SPINTAYLOR equations, which include higher-order spin corrections than the MSA treatment, and are more robust across the binary black hole (BBH) parameter space.

In this paper we present a new Phenom model, PHENOMXPNR, which combines the complementary features of PHENOMXPHM-SPINTAYLOR and PHENOMXO4A; the seamless integration of the two models over the full coalescence is achieved through a mapping between the double-spin inspiral precession dynamics and the single-spin NR-tuned model through the merger and ringdown, which we will describe below. This prescription is sufficient to capture the broad features of precession effects through merger, with the caveat that one must first identify the appropriate spin values at merger; the latter are taken from the numerical evolution of the PN spin-precession equations previously implemented in PHENOMXPHM-SPINTAYLOR.

We find that PHENOMXPNR is the most accurate IMR FD model for non-eccentric BBH gravitational wave signals, and as such it supersedes all of its predecessors. Additionally, it achieves comparable accuracy to complete IMR time-domain (TD) models for precessing signals, with particular improvement for heavy mass, approximately face-on binaries.

PHENOMXPNR is the first semi-analytic model to incorporate NR calibration in the precessing sector and the effect of mode-asymmetry while retaining the computational efficiency required by large scale parameter estimation studies, as e.g. gravitational wave event catalogs. This is aided by the choice to work in the FD, where it is straightforward to include information from all the spherical harmonic modes above a fixed cutoff frequency in the likelihood calculation. In contrast, TD waveform models require careful adjustments of their starting frequency to ensure that all non-negligible harmonics are in the detector’s frequency band. Finally, the model is available as open source code within LALSuite, and has been reviewed by the LVK.

After establishing the notation and conventions in Sec. II, we summarise the main technical aspects of the model in Sec. III. Model accuracy, benchmarks and applications to source property measurements are presented in Sec. IV, followed by our

conclusions in Sec. V.

II. NOTATION AND CONVENTIONS

In the absence of orbital eccentricity, black hole binaries with misaligned spins are described by eight intrinsic parameters: the component masses m_i and spin vectors \mathbf{S}_i . The total mass of the binary is given by $M = m_1 + m_2$ and serves as a scale parameter. We define the mass ratios $q = m_2/m_1 \leq 1$ and $Q = 1/q \geq 1$ in addition to the symmetric mass ratio $\eta = m_1 m_2 / (m_1 + m_2)^2$. The dimensionless spins are given by $\chi_i = \mathbf{S}_i / m_i^2$, where $|\chi_i| \in [0, 1]$ respects the Kerr limit.

It is often useful to decompose the spins into components parallel and perpendicular to the Newtonian orbital angular momentum \mathbf{L} ; $\chi_i^\parallel = \chi_i \cdot \hat{\mathbf{L}}$ and $\chi_i^\perp = \chi_i - \chi_i^\parallel \hat{\mathbf{L}}$, where the hat indicates the unit vector. It can also be useful to consider the combinations of the spin components as these dominate the effect of the spins on the waveform. The dominant contribution to the aligned-spin (the spins parallel to the orbital angular momentum) behaviour is parameterised by [37]

$$\chi_{\text{eff}} = \frac{m_1 \chi_1^\parallel + m_2 \chi_2^\parallel}{m_1 + m_2}, \quad (1)$$

while the effective precession spin [38]

$$\chi_p = S_p / m_1^2, \quad (2)$$

where $S_p = \frac{1}{A_1} \max(A_1 S_1^\perp, A_2 S_2^\perp)$, $A_1 = 2 + 3m_2/(2m_1)$ and $A_2 = 2 + 3m_1/(2m_2)$, captures the dominant contribution to the binary spin in the orbital plane.

III. MODEL OUTLINE

IMRPHENOMXPNR is a complete IMR gravitational wave model for quasi-circular precessing binaries of arbitrary total mass. The model uses results from PN theory during the inspiral, while the merger-ringdown portion of the signal is calibrated to NR. Precession effects complicate the modelling of gravitational wave signals, introducing oscillations into the amplitude and phase of the waveform. We therefore simplify modelling efforts by decomposing the waveform into the model for an aligned-spin binary and a frequency-dependent rotation which tracks the precession of the binary, as first proposed in Ref. [11]. This rotation is described by the Euler angles $\{\alpha, \beta, \gamma\}$ [12–14], which transform from the co-precessing frame to an inertial frame in which the total angular momentum of the binary is along the z -direction. The co-precessing model is based on the aligned-spin model PHENOMXHM [20], with modifications to the merger and ringdown. Additionally, multipole asymmetries are included in PHENOMXPNR. This co-precessing model follows the same procedure as presented in PHENOMXO4A [22]. The model for the angles α and β employs the SPINTAYLOR [16] prescription during the inspiral and a phenomenological description that has been calibrated to NR during merger and ringdown [35].

The PN inspiral prescription accounts for two-spin effects, while the calibration of the precessing sector to NR is performed against a catalogue of 80 single-spin precessing simulations where the spin is placed on the larger black hole [39].

We therefore require a mapping between the complete two-spin configuration and the single-spin calibration parameters. We outline the model in the following sections, recapping previous frameworks and highlighting recent developments.

A. Single spin mapping

We employ a single-spin mapping to go between the full two-spin description of a binary to the single-spin characterisation of the merger-ringdown used in the calibration of the model against NR. In the single-spin case, we characterise the binary's spins by the dimensionless magnitude χ and spin inclination θ_{LS} of the larger black hole, taking the smaller black hole to be non-spinning and ignoring in-plane spin rotation. We calculate these mapped merger-ringdown parameters at the frequency at which the merger-ringdown angles are computed. This transition frequency does not have a closed-form expression as a function of the binary's parameters, since it is related to the stopping frequency of the PN spin-precession equations. It is at this frequency that we compute the exact equivalent single-spin configuration required by the calibrated model for the Euler angles. This is given by

$$\chi = \sqrt{\chi_{\parallel}^2 + \chi_{\perp}^2}, \quad (3)$$

$$\cos \theta_{\text{LS}} = \frac{\chi_{\parallel}}{\chi}, \quad (4)$$

where

$$\chi_{\parallel} = \frac{M\chi_{\text{eff}}}{m_1}, \quad (5)$$

$$\chi_{\perp} = \frac{|\mathbf{S}_1^{\perp} + \mathbf{S}_2^{\perp}|}{m_1^2}, \quad (6)$$

and \mathbf{S}_i^{\perp} are the in-plane spin components. We employ χ_{eff} to capture the dominant behaviour of the aligned-spin contribution, which changes monotonically with time, but use the sum of the spin angular momenta at the transition frequency since we wish to capture the instantaneous value of the in-plane spin component, which varies sinusoidally as the spins combine constructively and destructively. Note that for close-to-equal mass binaries, χ can exceed the Kerr limit, since it is just a mapped parameter rather than a physical quantity.

This mapping is particularly important at small mass ratios, where the spins can be of equivalent magnitude and can therefore combine constructively or destructively, leading to strong or weak precession effects depending on the relative in-plane spin angles. For systems with unequal black holes masses, the spins rotate in the plane at different rates. It is therefore essential to employ the spin components immediately prior to merger in this calculation. At larger mass ratios, this mapping is equivalent to one using an average through the two-spin oscillations, as was employed in the PHENOMXO4A model. This improved single spin mapping allows us to capture two-spin effects through merger and ringdown without detailed additional calibration, as is demonstrated in Fig. 1.

Note that we retain the single-spin mapping employed in PHENOMXO4A as given in Eq. (19) of Ref. [36] for the antisymmetric part of the waveform. We explain this choice in sec. III C.

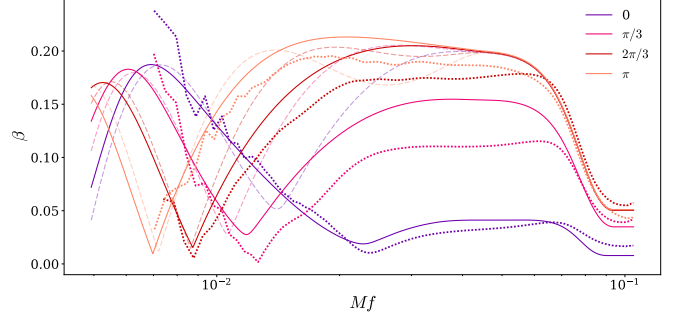


FIG. 1. Comparison of the Euler angle β between BAM NR simulations (dotted lines), PHENOMXO4A (dashed lines) and PHENOMXPNR (solid lines). We consider a set of 4 simulations with spin magnitudes $\chi_1 = 0.2$, $\chi_2 = 0.8$, both in-plane. In the simulation initial data, the spin on the primary is antiparallel to the separation $\mathbf{n} = \mathbf{r}_2 - \mathbf{r}_1$ between the black holes, while the spin at the secondary is rotated in-plane to have an angle of $\phi_1 = \{0, \pi/3, 2\pi/3, \pi\}$ with respect to the primary.

B. Co-precessing model

The co-precessing model employed in PHENOMXPNR follows closely that presented previously in PHENOMXO4A [22]. We employ the NR-calibrated aligned spin, higher multipole model PHENOMXHM [20] as the base model in the co-precessing frame. We include modifications to the late inspiral, merger and ringdown parts of the waveform that describe the effect of precession on the underlying co-precessing waveform and how the approximation that the co-precessing waveform can be described by the equivalent aligned-spin waveform breaks down. For the dominant $(2, \pm 2)$ multipoles these modifications are calibrated to NR simulations. We additionally include antisymmetric contributions to the $(2, \pm 2)$ multipoles. For the higher-order multipoles, the only modification is through an “effective ringdown frequency”, as detailed below.

The modifications to the symmetric part of the co-precessing waveform are described in detail in Sec. III A. 1. of Ref. [22]. In brief, deviations u_k are applied to each of the model coefficients λ_k describing the dominant multipole modelled in PHENOMXAS [15], giving the new value of the parameter

$$\lambda'_k = \lambda_k + \chi \sin(\theta_{\text{LS}}) u_k. \quad (7)$$

The subdominant multipoles are not calibrated directly. Instead, we adjust only the ringdown frequency, since the waveform is modelled in the co-precessing frame rather than that in which the ringdown frequencies are calculated when using perturbation theory. The ringdown frequency in the co-precessing frame $\omega'_{\ell m}$ is given by [40]

$$\omega'_{\ell m} = \omega_{\ell m} - m(1 - |\cos \beta_{\text{RD}}|)(\omega_{22} - \omega_{21}), \quad (8)$$

where $\omega_{\ell m}$ are the ringdown frequencies as calculated from perturbation theory and β_{RD} is the value to which the opening angle of the precession cone settles after merger.

Outside the calibration region we aim to ensure that the model varies smoothly across the parameter space and the behaviour is not pathological. We therefore employ the deviations to the aligned-spin waveform model parameters only up to $q = 20$. Beyond this mass ratio, we employ the PHENOMXAS waveform with the ringdown frequency still adjusted to be the effective ringdown frequency given in Eq. 8. The transition occurs smoothly over the range $q \in [10, 20]$.

C. Multipole asymmetries

For aligned-spin binaries, we have the reflection symmetry

$$h_{\ell,m} = (-1)^{\ell} h_{\ell,-m}^* \quad (9)$$

between the positive and negative m multipoles $h_{\ell,m}$. However, this symmetry is broken for systems with misaligned spins [41, 42], for which individual modes do not satisfy Eq. 9, irrespective of the frame in which they are expressed. Consequently, aligned-spin waveforms (which respect equatorial symmetry by construction) can only serve as an approximate description of gravitational wave multipoles in the co-precessing frame [18, 43]. The asymmetry between negative and positive m modes results in the emission of linear momentum perpendicular to the plane of the binary which can lead to large recoil velocities of the final black hole [41].

The asymmetry can be quantified as an anti-symmetric combination of the $\pm m$ modes for each (ℓ, m) . We include the dominant multipole asymmetry model of Ref. [36] in the coprecessing-frame and rotate to the inertial frame following Eqs. (18) and (19) of Ref. [22]. We give here a brief overview of this model for completeness and refer the reader to the aforementioned references for further details.

The complex, anti-symmetric FD waveform, $A_a(f)e^{i\phi_a(f)}$, is used to construct the dominant multipoles $h_{2,\pm 2}(f)$ in the coprecessing-frame as

$$h_{2,2}(f) = A_s(f)e^{-i\phi_s(f)} + A_a(f)e^{i\phi_a(f)}, \quad (10)$$

$$h_{2,-2}(f) = A_s(f)e^{i\phi_s(f)} - A_a(f)e^{-i\phi_a(f)}, \quad (11)$$

where A_s and ϕ_s represent the symmetric amplitude and phase respectively. The model for the anti-symmetric amplitude is of the form

$$A_a(f) = \kappa(f)A_s(f), \quad (12)$$

where $\kappa(f)$ is given by a PN estimate and an NR-calibrated correction. The anti-symmetric phase has an interesting structure, where it evolves differently from the symmetric phase in the inspiral [42] but quickly catches up with it near merger, as shown in Fig. 11 of Ref. [36]. Therefore, the anti-symmetric phase uses a piecewise construction

$$\phi_a(f) := \begin{cases} \frac{1}{2}\phi_s(f) + \alpha(f) & f < pf_{\text{RD}} \\ \phi_s(f) & f \geq pf_{\text{RD}} \end{cases}, \quad (13)$$

where $p \in [0, 1]$, to map the symmetric phase and the precession angle $\alpha(f)$ (described in Sec. III E) into $\phi_a(f)$. This feature becomes even more intriguing for higher multipoles and was first identified in Ref. [44]. The optimal choice of p and the different phase offsets, to ensure smooth transition in the phase, are obtained by calibrating to single-spin NR simulations and have been discussed in details in Sec. V of Ref. [36]

As noted in Sec. III A, we retain the single-spin mapping previously employed in PHENOMXO4A for the antisymmetric part of the waveform. The in-plane spin dependence of the anti-symmetric amplitude has been absorbed in the PN estimate of $\kappa(f)$, as is evident from Eq. (15) of Ref. [36]. The amplitude of the asymmetry depends only on the overall misaligned spin content and not on spin precession; therefore, employing the

instantaneous value of χ_{\perp} would not be particularly useful for the asymmetry model. Further, for near-equal-mass configurations, the spins can combine destructively to almost completely cancel at a given frequency and incorrectly suppress the asymmetry entirely. We therefore retain the previous mapping.

Comparisons of out-of-plane recoil velocities with the NR-SUR7DQ4 model revealed that the initial implementation of the asymmetry model in PHENOMXO4A neglected to account for the angle between the in-plane spin and separation vector at the reference frequency while constructing the anti-symmetric phase. Fixing this issue led to excellent agreement in recoil velocity estimates between the two models (cf. Fig. 4 and discussion in Sec. III C in Ref. [45]).

D. Final spin

The ringdown part of the model relies on the ringdown frequencies and damping times of the Quasinormal Modes (QNM) present in the waveform, as calculated from perturbation theory. These can be predicted for a given final mass and spin of the binary. The mass and spin of the remnant black hole formed from the corresponding aligned-spin binary are calculated using fits to numerical relativity, as in PHENOMX-PHM [46]. The mass of the remnant is largely unaffected by presence of in-plane spins, whereas the final spin of the remnant requires the addition of the in-plane component. Since the in-plane spins are conserved to leading order throughout the evolution of the binary, we calculate the final spin as

$$\chi_f = \text{sgn}(\cos \beta_{\text{RD}}) \sqrt{\left(\left(\frac{m_1}{M}\right)^2 \chi_{\perp}\right)^2 + (\chi_f^{\parallel})^2} \quad (14)$$

where χ_{\perp} is calculated using Eq. 6, using the reference spins. χ_f^{\parallel} is the value of the final spin predicted for the corresponding aligned-spin binary as given by Ref. [46]. Note that Eq. 14 differs from previous methods of estimating the final spin in the method used to determine the region of the parameter space in which the final spin changes sign. Previously, $\text{sgn}(\chi_f^{\parallel})$ was used; assuming that the direction of the final spin is consistent with the mapping to an aligned-spin system. Here, we instead take it to be given by $\text{sgn}(\cos \beta_{\text{RD}})$, which is instead predicated on the size of the opening angle of the precession cone during ringdown [40].

The choice to employ the sum of the in-plane spin components to calculate χ_{\perp} (as in Eq. 6) in the computation of the final spin magnitude yields a slightly more accurate estimate of the remnant spin than employing the precession-averaged χ_p , as done previously in PHENOMXO4A. This is illustrated in Fig. 2, where we compare the predictions of the surrogate model NRSUR7DQ4REMNANT with the approximations employed in PHENOMXO4A and PHENOMXPNR for a sample of 10000 BBH configurations, with $q \in [1, 5]$, $m_1 \in [20, 200]M_{\odot}$, spins isotropically distributed, and dimensionless spin magnitudes $\chi_{1,2} \leq 0.9$. For each configuration, the reference epoch of NRSUR7DQ4REMNANT is chosen in accordance with the spin reference frequency of the phenomenological models. The final spin predicted by PHENOMXPNR (PHENOMXO4A) has a median relative error of 0.8% (1%) with respect to the NR surrogate model.

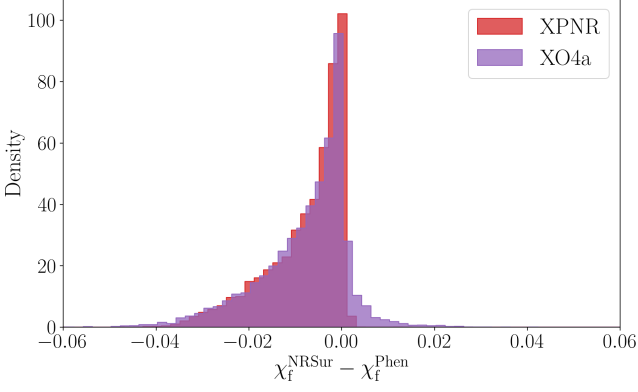


FIG. 2. Signed error on the remnant spin magnitudes predicted by IMRP_{PHENOM}XPNR (red) and IMRP_{PHENOM}XO4A (purple) with respect to the surrogate model NRSUR7DQ4REMNANT. The errors have been evaluated on a set of 10000 randomly drawn precessing BBHs. The final spin prescription employed by IMRP_{PHENOM}XPNR yields slightly improved results, which are especially visible in the right tail of the error distribution.

E. Angle model

To transform the co-precessing model into a complete model of a precessing waveform, we require a model for the precession angles $\{\alpha, \beta, \gamma\}$. The model presented here for α and β employs a PN prescription to describe the evolution of the precession dynamics through the inspiral and a phenomenological description calibrated to NR in the merger and ringdown. These two regions are then smoothly connected. The remaining precession angle γ is calculated numerically using the minimal rotation condition [14].

For the precession angles α and β , we use the SPINTAYLOR prescription during the inspiral, following the method described in [16]: after numerically evolving the PN orbit-averaged spin-precession equations in the TD, one obtains α and β as a function of frequency by means of the stationary phase approximation. In the current implementation of the model, we rely by default on the 3.5 PN SPINTAYLORT4 phasing, with 3 PN spin effects in the phasing and spin-precession equations. In the SPINTAYLOR model, the precessional motion is tracked by the time-evolution of the Newtonian orbital angular momentum: hence, we rescale β to ensure these angles describe the precessional motion of the optimal emission direction of the gravitational waves rather than of the plane of the binary. The rate of precession of the optimal emission direction during inspiral was shown in Ref. [35] to be consistent with the rate of precession of the Newtonian orbital angular momentum; consequently no further modification of the SPINTAYLOR prescription is required for α .

The merger-ringdown model for the angles is described in detail in Refs. [22] and [35]. The functional forms of α and β are

$$\alpha(f) - \langle \alpha(f) \rangle = - \left(\frac{A_1}{f} + \frac{A_2 \sqrt{A_3}}{A_3 + (f - A_4)^2} \right), \quad (15)$$

$$\beta(f) - \langle \beta(f) \rangle = \beta(f) - B_0 = \frac{B_1 + B_2 f + B_3 f^2}{1 + B_4 (f + B_5)^2}, \quad (16)$$

where A_i , B_i are functions of q , χ and θ_{LS} given in Eqs. (25)-(35) of Ref. [22] and $\langle \rangle$ indicates the mean value. The

coefficients in these ansatz are calibrated to a data set of 80 single-spin precessing BAM simulations [39]. We employ the improved spin-mapping detailed in Sec. III A in order to evaluate these coefficients for two-spin systems.

Outside the calibration region, the model for the merger-ringdown angles transitions smoothly to an analytic extension of the SPINTAYLOR angles. To do this we employ the windowing function described in Sec. IV. C of Ref. [22]. The analytic continuation of α is given by

$$\alpha(f) = - \left(\varepsilon_1 + \frac{\varepsilon_2}{f^2} + \frac{\varepsilon_3}{f^4} \right), \quad (17)$$

where the coefficients ε_i are determined by requiring that the ansatz match the SPINTAYLOR value of α at the two frequency points $0.97 f_{\text{max}}^{\text{PN}}$ and $0.99 f_{\text{max}}^{\text{PN}}$ and its derivative at the latter point. $f_{\text{max}}^{\text{PN}}$ is the maximum frequency to which the SPINTAYLOR integration can be performed. The analytic continuation of β is given by

$$\beta(f) = \frac{e^{-\kappa f}}{f^2} \left(\xi_1 + \frac{\xi_2}{f} + \frac{\xi_3}{f^2} \right) + \beta_{\text{RD}}, \quad (18)$$

where, as for α , the coefficients ξ_i are found from the requirement that the ansatz match the SPINTAYLOR value at two frequency points (here $0.97 f_{\text{max}}^{\text{PN}}$ and $0.98 f_{\text{max}}^{\text{PN}}$) and its derivative at the latter point. This ansatz ensures a smooth fall-off or rise to the value of β_{RD} . Previously, in the PHENOMXPHM-SPINTAYLOR model this value was given by 0 or π . However, we now use the fit to NR for the ringdown value of β given by Eq. (44) of Ref. [22]. The rate of decay is given by $\kappa = 2\pi \Delta f_{\text{damp}}$, where $\Delta f_{\text{damp}} = f_{\ell m}^{\text{damp}} - f_{22}^{\text{damp}}$ and $f_{\ell m}^{\text{damp}}$ is the damping frequency of a given QNM for a black hole with a given final mass and spin.

Inside the calibration region, where the calibrated model for the precession angles is employed, we ensure C^1 continuity by employing an intermediate region that matches the value and gradient of both the inspiral and merger-ringdown pieces at the connection frequencies.

For α , the connection is done as described in Sec. VIII A of Ref. [35]. We use an interpolating function of the form

$$\alpha(f) = a_0 f^2 + a_1 f + a_2 + \frac{a_3}{f}, \quad (19)$$

where the coefficients a_i are determined by requiring the interpolating function to be equal to the SPINTAYLOR value and gradient at the start of the intermediate region and to the merger-ringdown ansatz value and gradient at the end of the intermediate region.

The SPINTAYLOR angles do not always evaluate up to the frequency required to connect to the merger-ringdown model for β , which is given by Eq. (16). We therefore introduce a connection function

$$\beta(f) = b_0 + b_1 f + b_2 f^2 + b_3 f^3, \quad (20)$$

where the coefficients b_i are determined by requiring that their value and gradient is given by that of the PN β at the end of the integration of the angles and by those of Eq. 16 at the frequency at which the merger-ringdown ansatz is attached. We then treat this combined inspiral β as described in Sec. VIII B of Ref. [35] and summarised below.

First, we taper the oscillations seen in the PN prescription for the angles during the inspiral as they are not present in the late

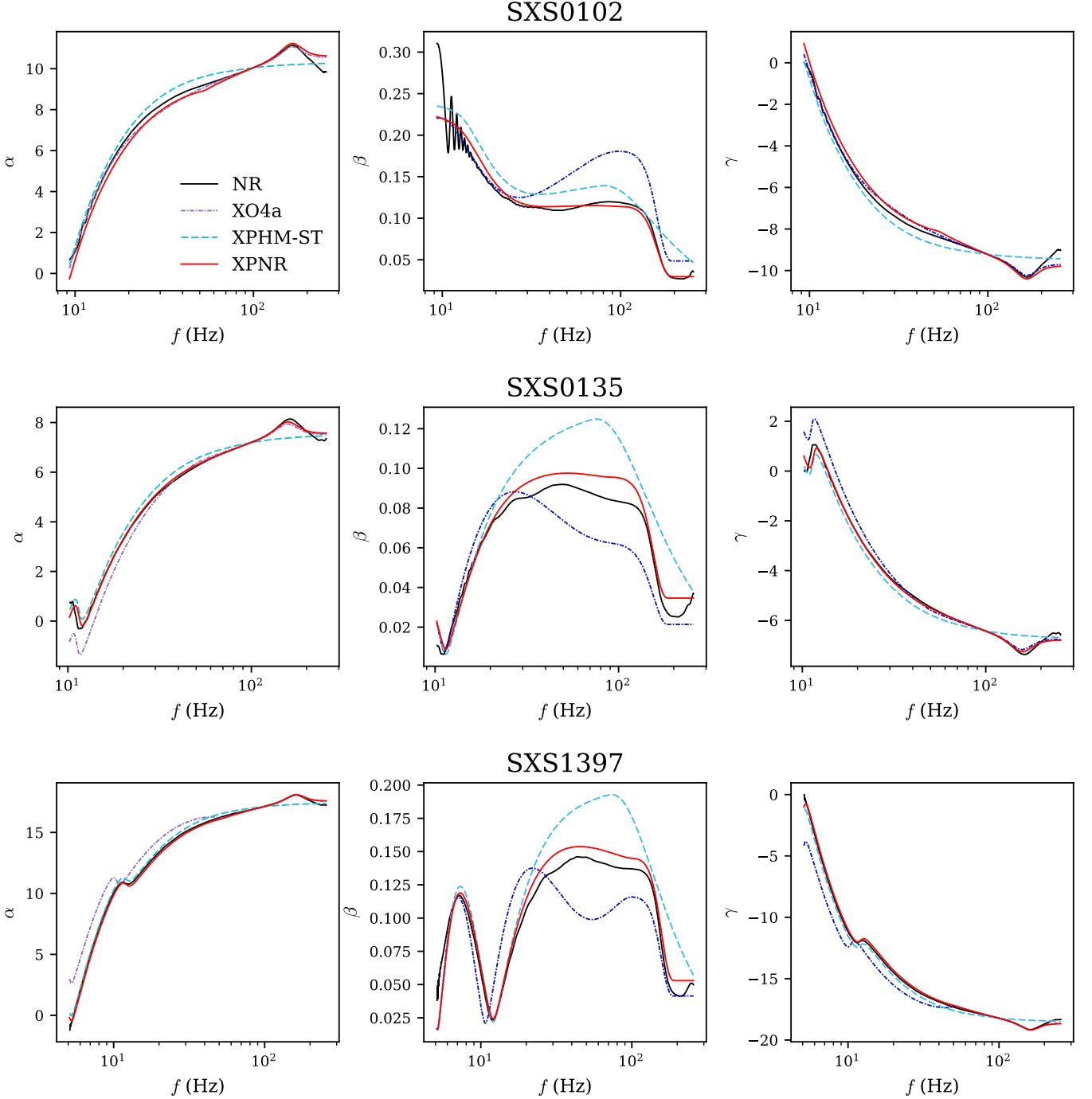


FIG. 3. Comparison of the new IMRPHENOMXPNR model angles with those for a selection of NR waveforms. We also compare the angles used in the previous models IMRPHENOMXPHM-SPINTAYLOR and IMRPHENOMXO4A. We consider three NR cases at close to equal mass taken from the SXS catalogue [47]. Their properties are detailed in Tab. I.

inspiral to merger regions of signals from NR simulations. Further, it ensures a smooth connection with the merger-ringdown ansatz. The tapered expression is then rescaled in order to find the value of β describing the precession cone given by the optimal emission direction of the gravitational wave signal, rather than that describing the evolution of the orbital angular momentum, as is returned by the SPINTAYLOR evolution of the angles. Finally, we apply an additional rescaling by multiplying through by an expression of the form

$$k(f) = 1 + k_1 f + k_2 f^2, \quad (21)$$

that leaves β invariant at low frequencies but ensures the value

of β and its derivative match at the connection frequency.

We transition smoothly beyond the calibration region over the range $q \in \{8.5, 12\}$ and $\chi \in \{0.85, 1.2\}$. To avoid the inclusion of pathologies in the fits outside the calibration region, we fix the values of the various coefficients $C_i \in \{A_i, B_i\}$ so that

$$C_i(\eta < \eta_b; \chi > \chi_b) = C_i(\eta = \eta_b; \chi = \chi_b), \quad (22)$$

where $\eta_b = 0.09$ and $\chi_b = 0.8 - 0.2 \exp[-((q - 6)/1.5)^8]$.

	q	\mathbf{S}_1	\mathbf{S}_2
SXS0102	1.50	(0.50, 0.00, 0.00)	(0.50, 0.00, 0.00)
SXS0135	1.64	(-0.09, 0.06, 0.02)	(0.11, -0.23, -0.23)
SXS1397	1.56	(0.22, 0.09, -0.18)	(-0.44, -0.16, 0.11)

TABLE I. Properties of NR cases considered in Fig. 3.

F. Extension to higher-order multipoles

In the frequency domain, we cannot simply transform the higher-order multipoles with the set of precession angles appropriate for the $(2, \pm 2)$ multipoles. Instead, we follow the prescription described in Ref. [48] and further developed in Ref. [22] and use a set of angles applicable for each set of multipoles with a given ℓ . The value of the higher multiple angles α and β are obtained by a frequency rescaling of the relevant angle model for the $\ell = 2$ multipoles. This operation mirrors the rescaling that is applied to the inspiral phasing of the subdominant modes to obtain their FD evolution in terms of that of the $(2, \pm 2)$ mode and rests on the same assumptions. At low frequencies, we employ the PN frequency rescaling

$$f \rightarrow \frac{2f}{m}, \quad (23)$$

while at high frequencies, we use the difference between the ringdown frequencies $f_{\ell m}^{\text{RD}}$ so

$$f \rightarrow f - (f_{\ell m}^{\text{RD}} - f_{22}^{\text{RD}}). \quad (24)$$

The final angle γ is then obtained for each new pair of angles $\{\alpha, \beta\}$ via the minimal rotation condition, as for the $\ell = 2$ angles.

IV. MODEL PERFORMANCE AND PARAMETER ESTIMATION

Combining the key features of the PHENOMXPHM-SPINTAYLOR model with those of PHENOMXO4a results in an improved description of the precessional dynamics of a binary system, as has been detailed above. In this section we demonstrate this improved description and explore the impact on the traditional measure of model accuracy –the mismatch– and on the model’s ability to accurately infer the parameters of a binary from a detected signal. We employ the definitions of the mismatch \mathcal{M} and precessing mismatch \mathcal{M}_W given in Sec. XI A of Ref. [35], employing the power spectral density of advanced LIGO at design sensitivity [49]. Finally, we consider the impact of these developments on the computational performance of the model.

A. Angle model accuracy

Employing the SPINTAYLOR angles improves the accuracy of the precessing waveform during inspiral, as has been demonstrated in Ref. [16]. In particular, the SPINTAYLOR angles capture the phasing of two-spin oscillations with greater accuracy than the MSA angles previously employed in models such as PHENOMXPHM-MSA and PHENOMXO4a. Further, since this approach involves the evolution of the precession dynamics, we are able to employ the values of the spins at merger in the

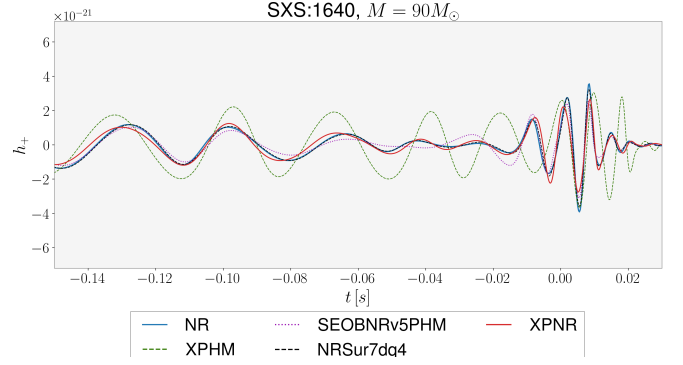


FIG. 4. TD comparisons between the NR simulation SXS:1640 and several time and FD waveform models, for an illustrative binary with total mass of $90 M_\odot$. The new model is plotted in red, and shows an excellent agreement with the underlying NR data (thick blue line).

single-spin mapping detailed in Sec. III A, rather than using the spins at the reference frequency. This ensures that the evaluation of the merger-ringdown ansatz, which relies on this mapping, is now significantly more accurate. The greatest improvement is seen for systems at close to equal mass where the two-spin oscillations are strongest and the approximate two-spin mapping employed in IMRPHENOMXO4a breaks down.

The improvement in the description of the precession dynamics from combining the SPINTAYLOR angles with the NR-informed merger-ringdown prescription is demonstrated in Fig. 3. Here we compare the angles extracted from NR simulations with those predicted by the three different models PHENOMXPHM-SPINTAYLOR, PHENOMXO4a and PHENOMXPNR for three cases taken from the SXS catalogue [47], details of which are given in Tab. I. It can clearly be seen that employing the SPINTAYLOR angles, as in PHENOMXPHM-SPINTAYLOR and PHENOMXPNR, results in a more accurate description of the oscillations from two-spin systems. Likewise, the inclusion of the calibration to NR in the merger-ringdown in PHENOMXO4a and PHENOMXPNR ensures we capture crucial features of the angles. For example, we capture the Lorentzian dip in the precession angle α and the rapid fall-off in β which settles down to a constant value. Crucially, the use of the SPINTAYLOR evolution of the spins to evaluate the merger-ringdown ansatz ensures an improved performance in the estimation of the magnitude of β at the start of the merger. This means that the opening angle of the precession cone, and consequently the relative amplitude of the subdominant multipoles relative to the dominant $\ell = m$ multipole will be correctly captured throughout the merger and ringdown.

This improvement in capturing the precession dynamics is translated to an overall improvement in the waveform. In Fig. 4, we plot the cross polarization for the SXS simulation SXS:1640 [47], picking a total mass of $90 M_\odot$, with $\iota = \pi/8$ and reference frequency $f_{\text{ref}} = 15$ Hz. We superimpose the NR waveform with the prediction of several waveform models; for FD waveforms, we first optimise over the reference phase and in-plane spins to find the best matching template. One can appreciate that PHENOMXPNR shows an agreement with NR that is comparable to state-of-the-art TD models, greatly improving upon the original version of PHENOMXPHM. Such reliable descriptions are essential for accurate measurements of the spin properties of high-mass binaries, such as GW190521 [50], where we see only the last few cycles

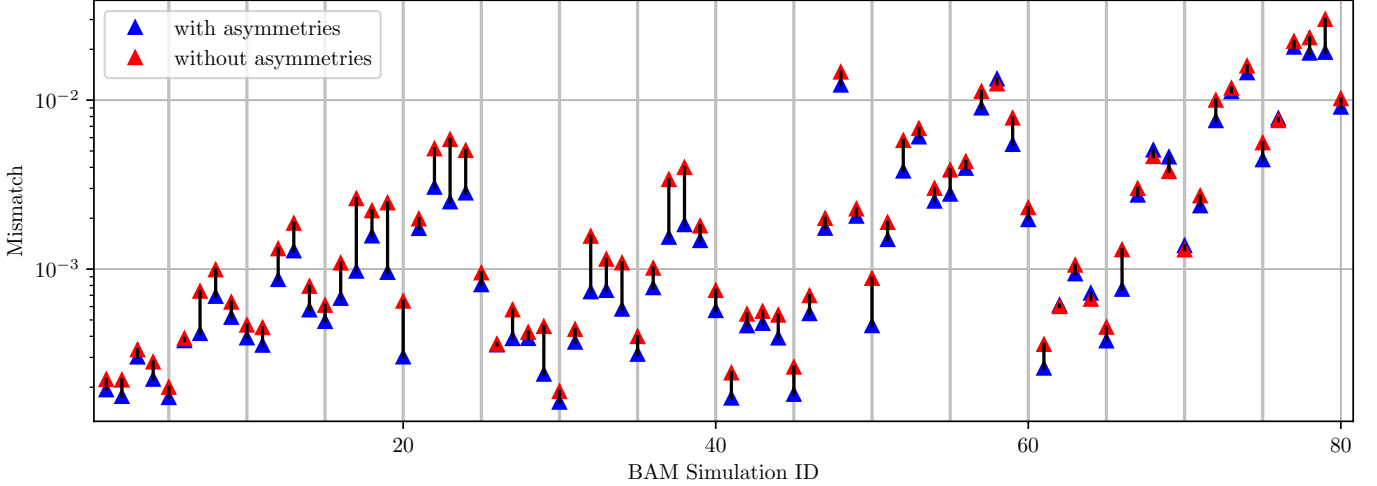


FIG. 5. Mismatch comparisons of IMRPHENOMXPNR against BAM NR simulations with (blue) and without (red) asymmetries. The x-axis shows the case identifiers for the NR simulations as used in the BAM catalog [39].

of the signal.

B. Asymmetry model accuracy

We demonstrate here the direct improvement to the model from the inclusion of mode asymmetries. While the improvement in model accuracy due to the inclusion of dominant multipole asymmetry in the coprecessing frame was reported for PHENOMXO4A [22], the extent to which this improvement carries over when transforming into the inertial frame has not been investigated before. We compute the mismatch between the model and the 80 BAM NR simulations [39] used in calibrating the model. We consider only the $(2, \pm 2)$ multipole in the co-precessing frame, since PHENOMXPNR includes asymmetries only in the dominant multipole. Furthermore, the inclusion of higher multipoles would make it harder to isolate the effects of the asymmetries.

The match is performed over the frequency range $f_{\min} = \max\{20, 1.35f_{\min}^{\text{NR}}\}$ Hz to $f_{\max} = 512$ Hz, where f_{\min}^{NR} is the starting frequency of the relevant NR waveform at a given total mass. We considered systems at two different total masses: $60M_{\odot}$ and $150M_{\odot}$ and a range of 5 equally spaced inclinations between 0 and π inclusive.

The results of this comparison are shown in Fig. 5, where we plot the simulations by their identifier in the BAM catalog. For visual reference, the values shown in this figure are averaged over total mass and inclination. The configurations shown here increase in mass ratio from left to right. Within each set of 20 simulations with the same mass ratio, the dimensionless spin magnitude increases. We can see the expected parameter space trend of increasing mismatch with increasing mass ratio and spin magnitude as the precession effects become stronger and modelling errors have greater impact. We demonstrate that the mismatches between PHENOMXPNR and the BAM NR simulations show noticeable improvement with the inclusion of mode asymmetries across the parameter space of calibration.

C. Mismatch comparisons

In order to assess the overall accuracy of the model, we computed the mismatch between the model and NRSUR7DQ4 for ~ 4100 binaries. We use NRSUR7DQ4 as a proxy for NR simulations as it enables us to obtain a more uniform coverage of the parameter space and within its calibration is typically an order of magnitude more accurate than other models [28]. We therefore do not expect modelling errors in NRSUR7DQ4 to dominate our assessment of our model performance.

We consider each system at a total mass of $\{60, 90, 120, 150\}M_{\odot}$ and at a range of six equally spaced inclinations between 0 and π inclusive. The intrinsic binary parameters are drawn from a uniform distribution over the calibration range of NRSUR7DQ4, sampling in the range of mass ratios $q \in \{0.25, 1\}$ and dimensionless spin magnitudes $\chi_i \in \{0, 0.8\}$. The match is performed over the frequency range $f_{\min} = \max\{20, 1.35f_{\min}^{\text{NRSur}}\}$ Hz to $f_{\max} = 512$ Hz, where f_{\min}^{NRSur} is the lowest starting frequency for NRSUR7DQ4 for a given configuration at a given total mass.

In order to assess whether the model is sufficiently accurate that we expect to see unbiased parameter recovery for a binary at a given signal-to-noise ratio (SNR), we consider a conservative distinguishability criterion [51]. For the measurement of a single parameter, we consider a 1-dimensional parameter space. We therefore require a mismatch $\mathfrak{M} < 1.35/\rho^2$ to be confident that the model will not be biased at 90% confidence for a given SNR ρ .

When considering only the dominant quadrupole contribution to the signal (i.e. the $\ell = 2$ multipoles) we find that the model performance is typically very good, as is shown in Fig. 6. 99.9, 90.9 and 71.8% of cases satisfy the distinguishability criterion for signals at an SNR of 10, 20 and 30 respectively. The model for the precession dynamics and the calibration of both the precession angles and the dominant multipole in the co-precessing frame is therefore performing well.

However, when considering the complete signal with all multipoles included in the model, the performance degrades slightly, as can be seen from Fig. 7, signalling we might need to reassess a number of our modelling assumptions for

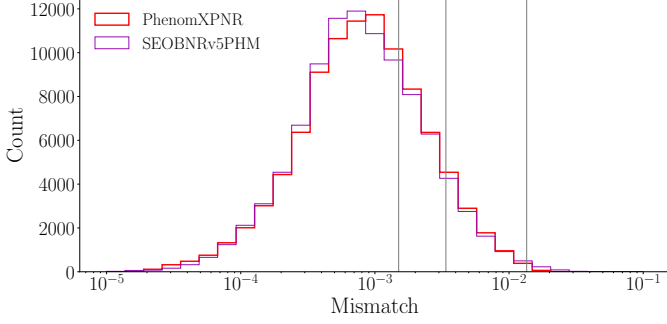


FIG. 6. Histogram showing the value of the mismatch value for ~ 4100 binaries. We compute the mismatch between our chosen model and NRSUR7DQ4. We consider only the $\ell = 2$ multipoles in the inertial frame. The grey lines give the mismatch threshold below which we are confident that the model should be unbiased at SNR 10, 20 and 30 (in order of decreasing mismatch) based on the distinguishability criterion.

precessing systems in the frequency domain. While the best performing cases in the low-mismatch tail are largely unaffected, the distribution now extends to much higher values of the mismatch ($\mathcal{O}(10^{-1})$) as opposed to $\mathcal{O}(10^{-2})$). 91.9, 62.8 and 37.9% of cases satisfy the distinguishability criterion for signals at an SNR of 10, 20 and 30 respectively. By contrast, for SEOBNRv5PHM, the best performing model shown in this figure, 99.1, 81.2 and 52.4% of cases satisfy the distinguishability criterion for signals at an SNR of 10, 20 and 30 respectively. We would therefore expect that, for signals above an SNR of 20, the parameter estimation recovery will be biased for all models displayed in this figure across a reasonable fraction of the parameter space. This is discussed further in Sec. IV D.

The relative performance of the difference models can be seen from Fig. 8, which shows the results shown in Fig. 7 as a direct model-by-model comparison for each binary configuration considered. As the distribution of points is largely symmetric about the diagonal line in all panels, we can see that the performance of all models is approximately equivalent. However, the slight over-preponderance of points below the diagonal line in the first three panels shows that on average PHENOMXPNR shows a minor improvement the three other models PHENOMXO4a, PHENOMXPHM-SPINTAYLOR and PHENOMTPHM. This is expected from combining the SPINTAYLOR evolution of the angles present in both PHENOMXPHM-SPINTAYLOR and PHENOMTPHM, which improves the model performance for lower mass binaries, with the calibration of the precession angles through merger and ringdown present in PHENOMXO4a, which improves the model performance for higher mass binaries. This minor improvement can be seen in mean of the distribution which goes from 0.00508 and 0.00485 for PHENOMXPHM-SPINTAYLOR and PHENOMXO4a respectively to 0.00468 for PHENOMXPNR. However, when comparing against SEOBNRv5PHM, we see that SEOBNRv5PHM does not extend to quite such high values as PHENOMXPNR and the other models. This can be best explained by considering the performance of the model with varying inclination.

The dependence of the mismatch on inclination for binaries with a total mass of $150M_{\odot}$ is shown in Fig. 9. It should be noted that for precessing binaries, the inclination ι , as measured by the angle between the orbital angular momentum and the line of sight to the binary, will vary over the evolution of

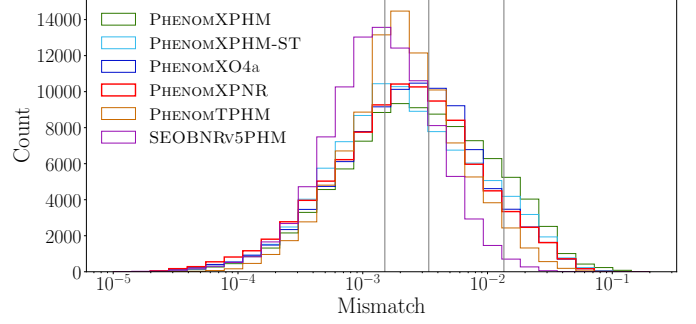


FIG. 7. Histogram showing the value of the mismatch value for ~ 4100 binaries. We compute the mismatch between our chosen model and NRSUR7DQ4. We consider all available multipoles in the inertial frame. The grey lines give the mismatch threshold below which we are confident that the model should be unbiased at SNR 10, 20 and 30 (in order of decreasing mismatch) based on the distinguishability criterion.

the binary as the orbital plane precesses. The values given here are therefore only true at the reference frequency. However, for the majority of cases considered here, the opening angle of the precession cone (β) will be sufficiently small as we are considering systems relatively close to equal mass. Therefore, it is reasonable to assume that the cases labelled $\iota = 0$ are close to face-on while those labelled $\iota = \pi/2$ are close to edge-on.

From Fig. 9 we can see that the improvements made to the model, and in particular the calibration of the co-precessing multipoles and merger-ringdown angles to NR, results in comparatively low mismatches for systems close to face-on. However, this improvement is lost as we move to considering systems close to edge-on where the higher multipoles have a greater contribution. This is due to the approximations made when extending the precession angles to higher-order multipoles as detailed in Sec. III F. These approximations are not required when modelling precession in the TD, as is done for SEOBNRv5PHM. It can clearly be seen that the performance of SEOBNRv5PHM is significantly less affected by the change in inclination than PHENOMXPNR and PHENOMXPHM-SPINTAYLOR. Consequently the relative performance of the models shifts as the inclination angle increases, with PHENOMXPNR the best performing model for “face-on” systems while SEOBNRv5PHM performs best for “edge-on” systems.

This degradation in model performance can also be seen when considering the performance of the model across parameter space, as is shown in Fig. 10. The model performs best for low-mass, low-precession signals with performance decreasing with increasing mass ratio and increasing value of χ_p . This is in part due to the decreased fidelity of the model of the precession dynamics for a more highly precessing system and in part due to the increased contribution of the higher-order multipoles to the waveform of such a system at any inclination.

Overall, we see that the model PHENOMXPNR is more accurate than either PHENOMXPHM-SPINTAYLOR and PHENOMXO4a and as such supersedes them as the most accurate FD model of precessing quasi-circular BBH systems currently available. However, the TD model SEOBNRv5PHM continues to perform better by a factor of 2 on average due to approximations which are made in the FD when modelling precessing systems which are not required in the TD. This is particularly relevant for systems with higher mass ratios and at higher inclinations. For heavy binaries at lower mass ra-

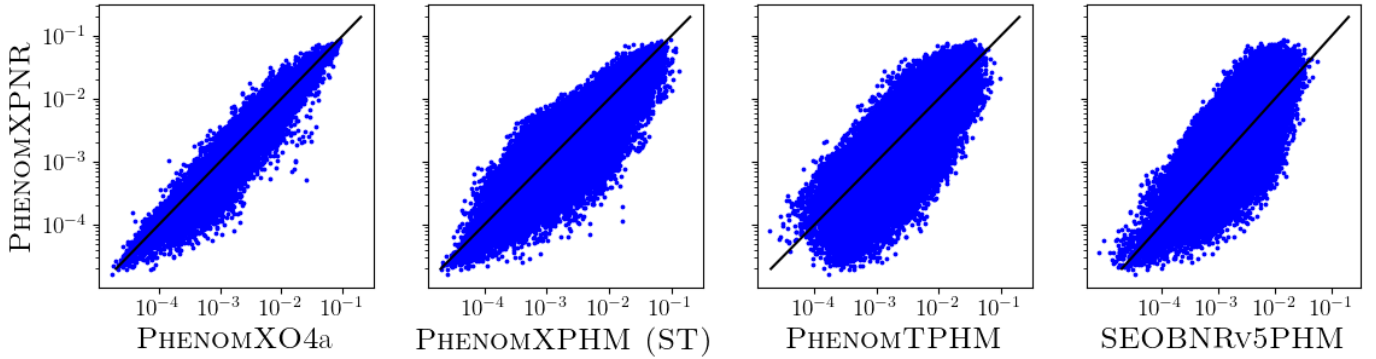


FIG. 8. Comparison of the performance of PHENOMXPNR with other models for precessing black-hole-binaries. We show the mismatch for all ~ 4100 binary configurations considered.

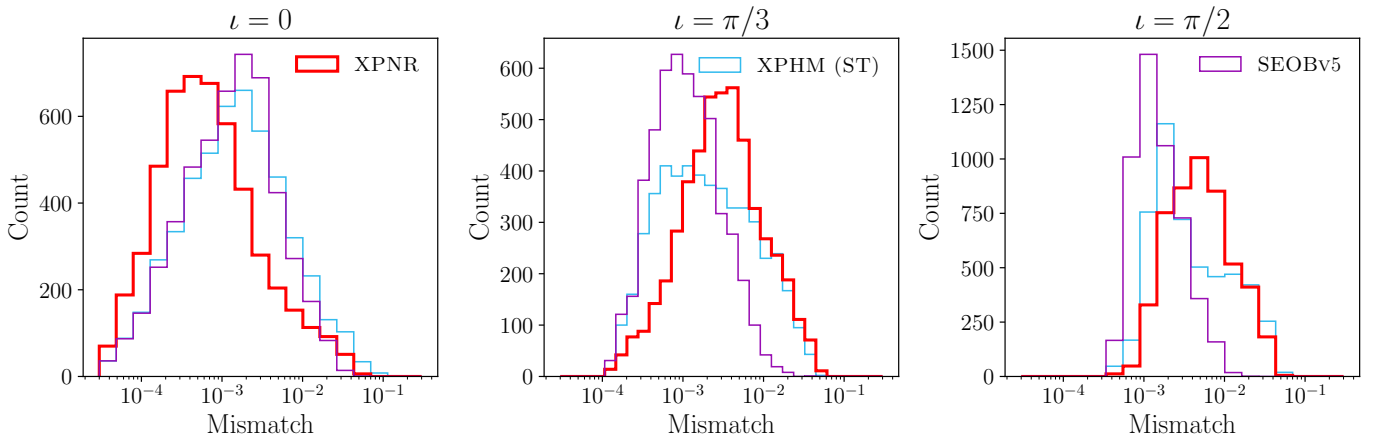


FIG. 9. We consider the variation in performance of three models, PHENOMXPNR, PHENOMXPHM-SPINTAYLOR and SEOBNRv5PHM, with inclination for high mass binaries ($150M_{\odot}$).

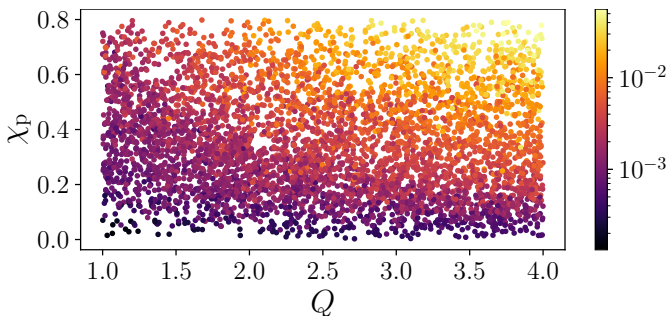


FIG. 10. Variation of the mismatch value averaged across all inclinations across parameter space for the model PHENOMXPNR. Model performance is best for systems with low mass ratios and low precession.

tios and close to face-on, PHENOMXPNR is the most accurate model considered here. The improved performance for low-inclination binaries is particularly pertinent as these are the systems we are most likely to observe with current detectors.

D. Parameter Estimation Results

To examine PHENOMXPNR's ability to infer the properties of a binary black hole merger, we perform Bayesian inference on gravitational wave data, d , comprised of either a simulated

or real gravitational wave signal, h , and noise, n ; Bayesian inference is the process of estimating the *posterior probability distribution*, which defines the probability of the binary having parameters λ given the gravitational wave data and model \mathbb{M} . The posterior is obtained through Bayes' theorem,

$$p(\lambda|d, \mathbb{M}) = \frac{\mathcal{L}(d|\lambda, \mathbb{M}) \Pi(\lambda|\mathbb{M})}{\mathcal{Z}}, \quad (25)$$

where $\mathcal{L}(d|\lambda, \mathbb{M})$ is the likelihood defined as the probability of the data given the binary parameters and model, $\Pi(\lambda|\mathbb{M})$ is the prior defined as the probability of the binary parameters given the model, and $\mathcal{Z} = \int \mathcal{L}(d|\lambda, \mathbb{M}) \Pi(\lambda|\mathbb{M}) d\lambda$ is the evidence. For a quasi-circular binary black hole merger, λ is a 15-dimensional vector: 8 dimensions quantifying the mass, m_i , and spin, \mathbf{S}_i , of each black hole, i , and 7 dimensions quantifying the source luminosity distance, sky location, merger time, phase, polarization and inclination angle.

In this work, we estimate the posterior probability distribution through stochastic sampling [52]. Specifically, we perform nested sampling [52] with DYNesty [53] via the BILBY library [54, 55]. When analysing real gravitational wave signals, we employ the same configuration and settings as those used by the LIGO–Virgo–KAGRA collaboration [56]. For all other analyses, we consistently used 1000 live points, the BILBY implemented RWALK sampling algorithm, and a theoretical power spectral density for Advanced LIGO's [57] and Advanced Virgo's [58] design sensitivity [59].

Unless otherwise stated, when analysing simulated gravita-

tional wave signals we take advantage of the zero-noise limit, defined as $n = 0$ for all times. A zero-noise analysis is the expected result when averaging over many different Gaussian noise realisations. By calculating and comparing the posterior distribution obtained for a range of different models in zero-noise, we can provide further insights into the accuracy of PHENOMXPNR; waveform differences can be probed directly and posteriors compared to the true source properties. We note that although a typical Bayesian analysis evaluates the model $O(10^7)$ times, we can only gain a limited insight into the performance of PHENOMXPNR over the vast 15-dimensional parameter space for a handful of injections. Also, although there have been recent efforts to explicitly incorporate the mismatch results in Fig. 7 into Bayesian inference techniques [60], we do not employ these techniques in this work.

1. Simulated gravitational wave signals

First, we assess the performance of PHENOMXPNR for gravitational wave simulations of known parameters. We pay particular attention to the improvement of PHENOMXPNR compared to its predecessor PHENOMXPHM-SPINTAYLOR to highlight the enhancements that we have implemented as part of this work. We consider two binary black hole systems where the properties differ from current population estimates [61]. The reason is because we expect the differences between models to be amplified in this region of the parameter space.

We consider a mass ratio $Q = 4$ NR simulation with a non-zero spin. We inject CF_54 provided by the BAM catalogue [39] with component masses $m_1 = 48 M_\odot$ and $m_2 = 12 M_\odot$, primary spin magnitude $a_1 = 0.6$ tilted at angle $\theta_1 = 2\pi/3$ rad and a secondary spin of 0. The inclination angle was defined to be $\theta_{\text{JN}} = 0.66$ rad, and the SNR was chosen to be $\rho = 20$. This simulation was selected since we observed an order of magnitude better performance (in terms of mismatches) for PHENOMXPNR compared to PHENOMXPHM-SPINTAYLOR and PHENOMXO4A. For this simulation we calculated mismatches: 0.008, 0.015, 0.016, 0.005, 0.004 for PHENOMXPNR, PHENOMXPHM-SPINTAYLOR, PHENOMXO4A, SEOBNRv5PHM and NRSUR7DQ4 respectively. Based on these mismatches, we would naively expect PHENOMXPNR, SEOBNRv5PHM and NRSUR7DQ4 to perform optimally for this system.

In Fig. 11 we see that PHENOMXPNR recovers the effective spins of the binary within the 90% confidence region, while PHENOMXPHM-SPINTAYLOR misidentifies the amount of precession in the binary: PHENOMXPHM-SPINTAYLOR infers greater support for a binary with spins aligned with the orbital angular momentum (smaller χ_p). We understand that NR-tuned co-precessing dominant mode inherited from PHENOMXO4A is the primary reason behind PHENOMXPNR's improvement in the recovered effective precessing spin: when we turn off the NR tuning for the co-precessing dominant mode we obtain a posterior distributions that is in better agreement with the PHENOMXPHM-SPINTAYLOR result. This is why PHENOMXPNR and PHENOMXO4A recover comparable distributions for this injection. When comparing Bayesian evidences, we see that the data prefers PHENOMXPNR over PHENOMXPHM-SPINTAYLOR by a factor of 3:1. We also analysed this injection with the NRSUR7DQ4 and SEOBNRv5PHM models. In general, NRSUR7DQ4 and SEOBNRv5PHM more

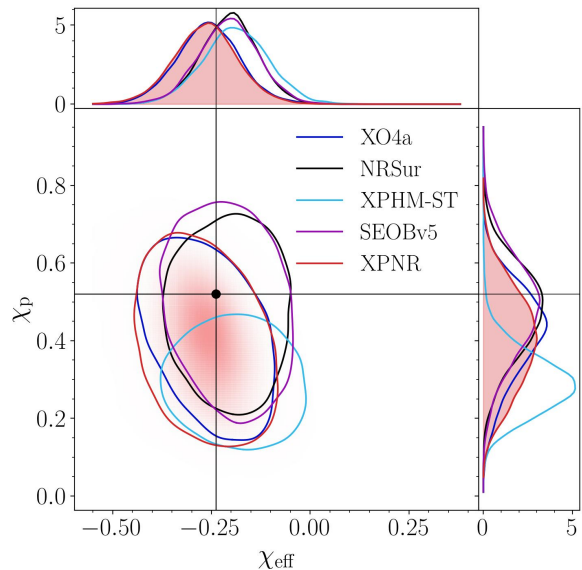


FIG. 11. Comparison between the two-dimensional marginalized posterior distributions for the effective parallel spin χ_{eff} and effective perpendicular spin χ_p when analysing the CF_54 numerical relativity simulation [39]. The contours encase 90% probability. The black crosshairs show the true values.

accurately capture the true source properties, with SEOBNRv5PHM closely resembling NRSUR7DQ4 for this analysis. We see that PHENOMXPNR agrees better with NRSUR7DQ4 and SEOBNRv5PHM than PHENOMXPHM-SPINTAYLOR.

Next, we inject a gravitational wave signal produced by a high mass binary black hole system. We chose to analyse this region of the parameter space since it enables a direct study of the merger/ringdown portion of the gravitational wave signal, allowing us to gauge the effects of the improved merger/ringdown prescription in PHENOMXPNR over PHENOMXPHM-SPINTAYLOR. We simulate a binary black hole merger with component masses $m_1 = 100 M_\odot$ and $m_2 = 50 M_\odot$, primary and secondary spin magnitudes $a_1 = a_2 = 0.8$ with tilts $\theta_1 = 1.2$ rad and $\theta_2 = 1.5$ rad for the primary and secondary spin vector respectively. The inclination angle was defined to be $\theta_{\text{JN}} = 0.45$ rad, and the SNR was chosen to be 50. Although the SNR is high, it remains less than the expected SNR at which GW150914 [9, 62] would have been observed with O4a-like detector sensitivities (~ 70) [63]. We generate the gravitational wave signal with NRSUR7DQ4.

In Fig. 12 we see that PHENOMXPNR more accurately captures the binary's total mass and mass ratio; all other models considered infer a higher total mass binary with more symmetric component masses. Interestingly, PHENOMXPNR and PHENOMXPHM-SPINTAYLOR recover disjoint distributions, with both PHENOMXPHM-SPINTAYLOR and SEOBNRv5PHM failing to recover the true source masses. When comparing PHENOMXPNR to PHENOMXO4A, we see that the additional improvements outlined in this paper lead directly to a tighter distribution around the true source masses. Finally, PHENOMXPNR more accurately captures the binary's true mass ratio and total mass than NRSUR7DQ4 despite the simulation being made with NRSUR7DQ4. We highlight that although

PHENOMXPNR performs better in this two-dimensional slice, the posterior is fifteen dimensional and overall NRSUR7DQ4 fits the data better than PHENOMXPNR. This can be seen by the larger Bayesian evidences for NRSUR7DQ4 compared to PHENOMXPNR.

The improved performance of PHENOMXPNR compared to the other models for this simulation correlates directly with the improved mismatch calculations. We find that PHENOMXPNR obtains a mismatch of 0.003 when comparing to the injection at the same fiducial parameters. This compares to 0.033 for PHENOMXPHM-SPINTAYLOR and 0.026 for SEOBNRv5PHM – both an order of magnitude larger than PHENOMXPNR – and 0.002 for PhenomXO4a. Assuming the commonly used distinguishability criterion from Ref. [51] (although we note that this is a conservative metric [64]), two waveforms are indistinguishable if their mismatch is below 0.003 for an SNR 50 GW signal (assuming 8 degrees of freedom). It is therefore unsurprising that PHENOMXPNR and PHENOMXO4A are the only models¹ to infer unbiased source estimates.

The observed waveform systematics in Fig. 12 implies that care must be taken when analysing high mass binary black hole systems with significant in-plane spin at large SNRs. Although astrophysically interesting, estimates for the black hole masses may differ depending on the model selected when performing inference. We note that this conclusion is dependent on the SNR of the injected signals. The inferred 90% confidence interval of each waveform model inversely scales with SNR: a wider posterior will be obtained for a lower SNR injection. Therefore, if the SNR is reduced we would expect better agreement between waveform models, with more models encasing the injected value within the 90% confidence interval. However, the maximum likelihood estimate, and posterior median should remain unchanged.

Although not shown here, we also verified the performance of PHENOMXPNR for 100 randomly chosen gravitational wave signals drawn from the prior distribution. We generated these simulations with PHENOMXPNR, injected the signals into different instances of Gaussian noise for a network of two Advanced LIGO detectors [57] and one Advanced Virgo detector [58], and assumed a duration of 8 seconds of data. When comparing the inferred posterior distributions against the injected values, we obtain the expectations from a Gaussian likelihood – an approximately linear relationship for each dimension.

2. Observed gravitational wave signals

Next we consider the performance of PHENOMXPNR for real gravitational wave signals. We analyse two signals that show waveform systematics between published posterior distributions, and have claimed evidence for precession of the orbital plane [66, 67]: GW190412 [65, 68] and GW200129 [32, 69]².

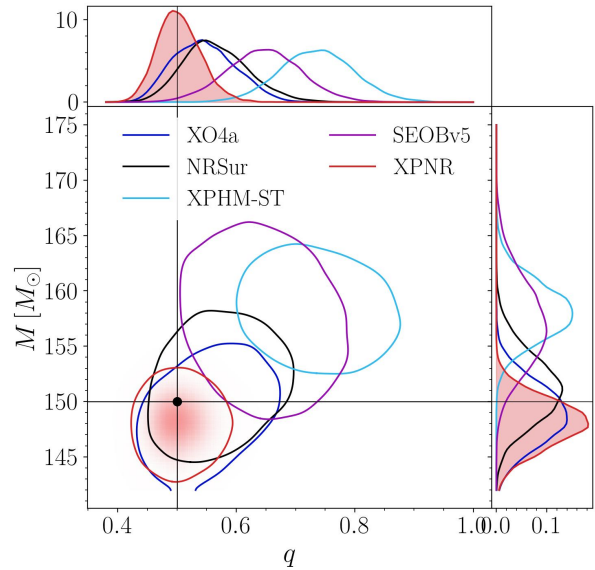


FIG. 12. Comparison between the two-dimensional marginalized posterior distributions for the binary total mass M and mass ratio q when analysing an NRSUR7DQ4 injection. The contours encase 90% probability. The black cross hairs show the true values.

These signals are therefore natural choices to test PHENOMXPNR's improved precession modelling and to check it's consistency with other state-of-the-art models.

In the left panel of Fig. 13 we show the inferred effective aligned spin χ_{eff} and mass ratio q for GW190412. We compare the posterior obtained with PHENOMXPNR to SEOBNRv5PHM and the published results by the LIGO–Virgo–KAGRA collaboration [65]; the LVK published results with PHENOMPv3HM [48], labelled *Phenom PHM*, and SEOBNRv4PHM [75], labelled *EOBNR PHM*. When restricting attention to the results published by the LIGO–Virgo–KAGRA collaboration, we see possible waveform systematics with *Phenom PHM* preferring more equal mass ratios and lower aligned spin than *EOBNR PHM*. We see that the observed systematics are no longer present amongst the latest generation of Phenom and SEOB models: PHENOMXPNR and SEOBNRv5PHM show good agreement with both inferring overlapping mass ratio and aligned spin probability densities. This corroborates the findings in Ref. [76], which highlighted that even for the non-precessing parameter space, the PHENOMX family of waveform models removes the observed systematics in GW190412 owing to the calibration to NR of the higher order multipoles.

In the right panel of Fig. 13 we show the inferred effective aligned spin χ_{eff} and effective precessing spin χ_p for GW200129. We see that PHENOMXPNR and SEOBNRv5PHM agree well, but both infer less precession than NRSUR7DQ4 and PHENOMXPHM-SPINTAYLOR.

Recently, Refs. [44, 77] showed that the evidence for precession in GW200129 increases when higher-order multipole asymmetries are included in the waveform model. Indeed, Ref. [44] specifically showed that the inferred χ_p more closely resembles the NRSUR7DQ4 result when higher-order multipole asymmetries are included in SEOBNRv5PHM. Given that PHENOMXPNR includes only the dominant contribution to the

¹ Aside from NRSUR7DQ4, which has a mismatch of exactly 0, since this model was used to generate the injection.

² We note that the evidence for precession in GW200129 has been argued against in previous work owing to noise artefacts at the time of GW200129 [70], although see Ref. [71] for a counter argument which claims that the evidence for precession remains after improved data cleaning, and claims that the binary may be eccentric [72–74].

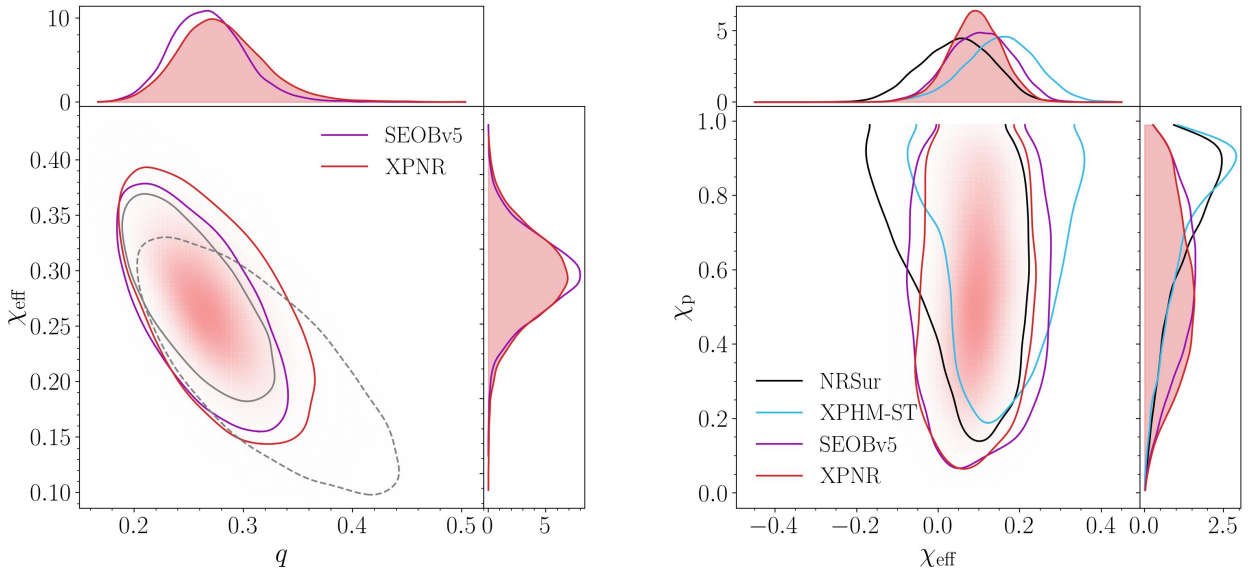


FIG. 13. Comparison between posterior distributions obtained when analysing real gravitational wave events. In the *Left* panel we show the two-dimensional marginalized posterior distribution for the mass ratio q and effective parallel spin χ_{eff} when analysing GW190412 [65]. We additionally show the *Phenom PHM* and *EOBNR PHM* posterior distributions reported in Ref. [65] in grey dashed and grey solid respectively. In the *Right* panel, we show the two-dimensional marginalized posterior distribution for the effective parallel spin χ_{eff} and effective perpendicular spin χ_p when analysing GW200129 [32]. In both cases, the contours encase 90% probability.

multipole asymmetries, the smaller χ_p measurement implies that higher-order contributions may be needed to reproduce the high precession result. This being said, PHENOMXPHM-SPINTAYLOR does not include multipole asymmetries but still measures a large χ_p . Interestingly, PHENOMXPHM-MSA also infers a large χ_p . We are unsure of the cause of this discrepancy.

Based on Bayesian analyses that we performed as part of this study, we see that PHENOMXPNR generally performs better than its predecessor PHENOMXPHM-SPINTAYLOR. We understand that PHENOMXPNR either agrees well with SEOB-NRv5PHM or performs better, particularly in the high mass parameter space. This correlates with the mismatch results presented in Sec. IV C.

E. Timing tests

In this section we compare waveform evaluation times between multiple members of the PHENOM waveform family. We first compute the evaluation time for a fiducial binary configuration with $Q = 3$, $\chi_1 = (0.2, 0, 0.3)$ and $\chi_2 = (0, -0.5, -0.4)$, generated on an Apple M2 Max MacBook Pro laptop across a frequency range spanning 20–2048 Hz and averaged over 50 waveform evaluations with identical parameters. This comparison is performed both across a range of total masses, ranging between 20–500 M_\odot as shown in the left panel of Fig. 14, and for a fixed total mass of 50 M_\odot and across a range of frequency step sizes df , shown in the right panel of the same figure. We compare the timing of four waveform models: PHENOMXPNR, PHENOMXO4a, PHENOMXPNR-ST and PHENOMXPHM-MSA.

The results shown in Fig. 14 display a clear trend of increasing waveform evaluation time across the four models that is

largely independent of total mass for this fiducial configuration, with PHENOMXPNR being the slowest model to evaluate and PHENOMXPHM-MSA the fastest. We also observe that at higher total masses, PHENOMXPHM-SPINTAYLOR differs from both of the approximants that use the inspiral MSA angles, and this timing performance is inherited by PHENOMXPNR. When df is varied, we see that for small frequency step sizes the models separate into those that use the tailored frequency spacing for the inspiral precession angle interpolation, detailed in Ref. [22], and those which do not use this frequency spacing for the precession angles.

We further investigate the timing performance of PHENOMXPNR in comparison to PHENOMXPHM-SPINTAYLOR broadly across the two-spin precession parameter space, run on the same hardware as the above analysis. We randomly sample 10,000 points across $Q \in [1, 10]$, $M \in [20, 150] M_\odot$, and spin orientations drawn uniformly in $\cos \theta_{\text{LS}} \in [-1, 1]$, uniformly in spin azimuthal angle between $[0, 2\pi]$, and spin magnitudes ranging uniformly from 0 to 1. These signals are generated across a frequency range of 20–1024 Hz for sake of memory and efficiency, and sampled at an appropriate frequency step size for the masses and spins of the given random point, which we produce using an estimate of the signal chirp time from the LALSIMULATION function XLALSimInspiralChirpTimeBound.

Figure 15 shows the results for the (\log_{10}) ratio of the timings for PHENOMXPNR and PHENOMXPHM-SPINTAYLOR, averaged over 3 waveform evaluations. The timing ratios show no dependence on any intrinsic parameters except for Q and M , so we restrict to plotting only points across the total mass and mass-ratio range of evaluation. We identify timing ratios greater than one, *i.e.*, when the evaluation of PHENOMXPNR is slower than PHENOMXPHM-SPINTAYLOR, with red circles in the plot, and blue triangles for points where the timing ra-

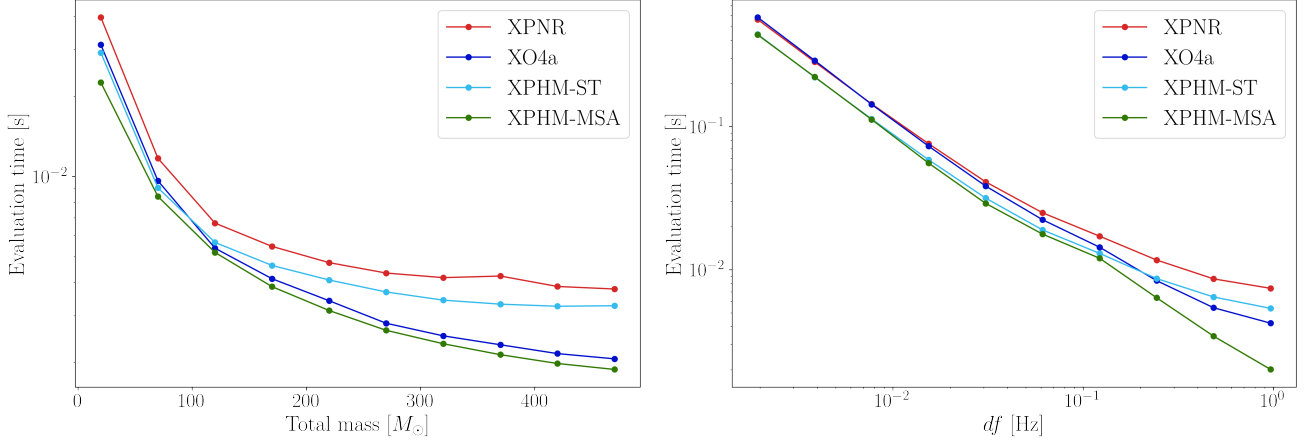


FIG. 14. Waveform evaluation timing for four different FD models: PHENOMXPNR, PHENOMXO4a, PHENOMXPHM-SPINTAYLOR and PHENOMXPHM-MSA. All timings were generated for a fixed binary configuration with $q = 3$, $\chi_1 = (0.2, 0, 0.3)$ and $\chi_2 = (0, -0.5, -0.4)$ produced between 20–2048 Hz. The left panel of the figure shows waveform evaluation times computed for a range of total masses between 20–500 M_\odot with a fixed frequency interval $df = 0.125$ Hz. The right panel displays runtime as a function of frequency spacing df for a fixed total mass of 50 M_\odot . All evaluation times are averaged over 50 waveform generations.

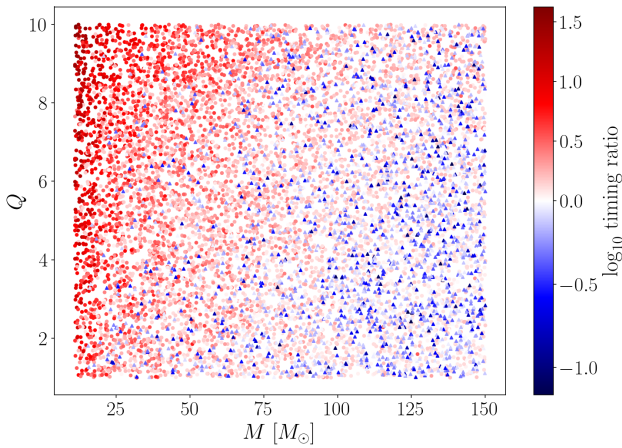


FIG. 15. We compare the runtime evaluation between two models, PHENOMXPNR and PHENOMXPHM-SPINTAYLOR, for a set of 10,000 points randomly drawn across the quasi-circular precessing parameter space. This figure shows the (\log_{10}) timing ratio of PHENOMXPNR to PHENOMXPHM-SPINTAYLOR plotted for the total mass M and mass-ratio Q , with values greater than zero denoting a longer runtime for PHENOMXPNR compared to PHENOMXPHM-SPINTAYLOR (the red circles) and values less than zero denoting a faster runtime (the blue triangles).

ratio is less than one. From Fig. 15 it is clear that the runtime performance of PHENOMXPNR depends most strongly on the total mass of the system, with the transition mass across unity in the timing ratio weakly depending on the mass-ratio. The slower waveform evaluation at lower total masses arises from the finer frequency sampling used to generate the interpolants for the precession inspiral angles to properly account for two-spin oscillations, again detailed in Ref. [22].

Finally we investigate the likelihood evaluation time of PHENOMXPNR compared to multiple members of the PHENOM waveform family. Given that the likelihood is evaluated $O(10^7)$ times in a typical Bayesian analysis, small differences in timing can significantly impact the efficiency of a Bayesian inference analysis. We calculate the evaluation time by taking

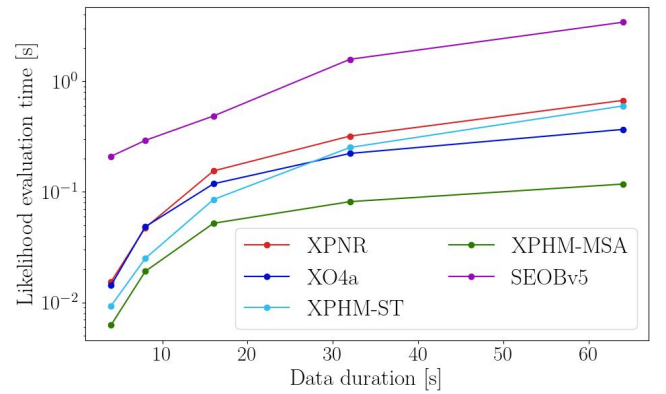


FIG. 16. Comparison between likelihood evaluation times for varying data duration. We compare the evaluation times for four different FD models: PHENOMXPNR, PHENOMXO4a, PHENOMXPHM-SPINTAYLOR, and the TD model: SEOBv5PHM. Each data point represents the mean of 10,000 likelihood evaluations calculated via BILBY. Binary parameters were drawn from priors distributions that cut the chirp mass parameter space to ensure that the gravitational waves fit within the specified data duration: larger data durations correspond to smaller chirp mass binaries.

the mean of 10,000 likelihood evaluations for different binary parameters λ calculated via BILBY; λ is randomly drawn from an agnostic prior distribution, with chirp mass cuts applied to ensure that the gravitational wave signal fits within the specified data duration. We enforce chirp masses between $25 \leq \mathcal{M} \leq 50$, $10 \leq \mathcal{M} \leq 25$, $6 \leq \mathcal{M} \leq 10$, $4 \leq \mathcal{M} \leq 6$, and $2 \leq \mathcal{M} \leq 4$ for the 4, 8, 16, 32, and 64 second data durations, respectively³. Since we are uninterested in the value of the likelihood, d is randomly generated Gaussian noise containing no signal. Each model evaluates the likelihood for the exact same binary configurations. All likelihood evaluations

³ Although the 32 and 64 second data durations contain binaries with masses consistent with the observed neutron star population, we ignored potential tidal affects and assumed that all binary components were black holes.

were performed on the same Lenovo AMD EPYC 7H12 node.

In Fig. 16 we see that the likelihood evaluation time increases for larger data durations. This is expected as the waveform evaluation time is longer for lower total mass binaries (see Fig. 14), and larger data durations are needed to encase lower total mass binaries. We see that for small data durations (< 10 seconds), PHENOMXPNR and PHENOMXO4a have comparable likelihood evaluation times, meaning that the extra physics added from the PHENOMXO4a model dominates the computational cost of PHENOMXPNR. As the data duration increases, PHENOMXPNR's likelihood evaluation time transitions from being dominated by the PHENOMXO4a model, to being dominated by the SPINTAYLOR evolution of the inspiral precession angles from PHENOMXPHM-SPINTAYLOR. This transition occurs at around a data duration of 30 seconds. We note that for these longer data durations the whittle likelihood will unlikely be used in Bayesian analyses; longer data duration analyses are more likely to use the Reduced Order Quadrature [78, 79] or multibanded likelihood [80] to reduce overall computational cost. The likelihood evaluation time for these long data durations are therefore unlikely to translate to the CPU time of typical analyses. Across the whole space, PHENOMXPNR is at most $1.9\times$ times slower than PHENOMXPHM-SPINTAYLOR per likelihood evaluation. When averaging across all data durations considered, PHENOMXPNR is $1.5\times$ times slower than PHENOMXPHM-SPINTAYLOR. We also performed the same analysis with SEOBNRv5PHM and found that PHENOMXPNR is at least $3.1\times$ times faster than SEOBNRv5PHM per likelihood evaluation. Similarly, when averaging across all data durations considered, PHENOMXPNR is $6.6\times$ times faster than SEOBNRv5PHM.

V. CONCLUSIONS

In this work, we have introduced PHENOMXPNR, a new gravitational wave model for BBH mergers that accurately captures precessional effects in quasi-circular inspirals. Our new model seamlessly combines several efforts aimed at capturing precessional signatures in gravitational wave signals: an accurate representation of the inspiral precession dynamics [16], a phenomenological description of the asymmetry between the $(2, 2)$ and $(2, -2)$ multipoles of the gravitational wave emission [36] and NR-calibrated models for the co-precessing frame multipoles and Euler angles accounting for precession effects in the merger-ringdown [35, 40].

We have provided a comprehensive overview of the different ingredients of the model in Sec. III, where we have summarised the salient features of PHENOMXO4A [22] and PHENOMXPHM-SPINTAYLOR [16], as well as the technical aspects involved in blending them together.

We then proceeded to provide quantitative measures of the enhanced performance of the model (Sec. IV). In Sec. IV A, we demonstrated that the Euler angles predicted by PHENOMXPNR better reproduce the ones extracted from NR simulations, significantly improving upon previous approximations. In Sec. ??, we have demonstrated that the inclusion of asymmetry in the dominant multipole consistently improves the accuracy of the model. In Sec. IV C, we have presented an extensive mismatch study against NRSUR7DQ4, showing that PHENOMXPNR is currently the most accurate semi-analytical waveform model for face-on/off precessing quasi-circular binaries. We

have then reinforced these conclusions through selected parameter estimation studies, outlined in Sec. IV D. We analysed both simulated signals with known source properties and real gravitational wave events. From the simulated signals, we have seen that, while all models can show biases in certain regions of the parameter space, there are regions where, for high mass signals, the additional NR calibration in PHENOMXPNR enables it to correctly infer the correct source properties while models lacking this calibration exclude the correct values at 90% confidence. From the detected signals we can infer that PHENOMXPNR performs reasonably when analysing real data. Including additional physics or improving the accuracy of the current models increases the agreement between models for a given event, but current model differences still lead to discrepancies when analysing more challenging signals. Finally, we have tested the performance of our model and compared it to previous precessing approximants, concluding that the improvements to model accuracy presented in this paper have resulted in a moderate decrease in efficiency. However, we can see that PHENOMXPNR is still appreciably more efficient than current state-of-the-art time domain models.

Overall, this model marks a significant step toward accurate and computationally efficient waveform models for precessing BBH systems, providing a new tool to perform inference of spin-precession effects in gravitational wave detections and probe the astrophysical origin and evolution of compact binaries. There are several key improvements that would further enhance the performance of PHENOMXPNR, such as modelling the asymmetry between $\pm m$ modes for the full mode content of PhenomX, tuning the merger-ringdown Euler angles to two-spin NR simulations, including more accurate estimates for the final mass and spin of the remnant [81] and increasing the faithfulness of the model for sources with non-negligible inclination, by reassessing the modelling assumptions made for the higher harmonics of precessing systems in the FD. Another potential extension of PhenomX templates would be the addition of other subdominant harmonics in the co-precessing frame, in particular of those carrying information about memory effects like the $(2, 0)$ mode [82, 83].

In the future, the insights gained in the construction of PHENOMXPNR will be utilised to improve the precessing TD model PHENOMTPHM. TD models offer a more intuitive picture of complex phenomena like precession or eccentricity and can greatly facilitate the construction of fully generic IMR templates including both [84]; they can also find important applications in the context of data analysis for space-borne interferometry, where the use of TD response functions can naturally accommodate realistic LISA orbital information [85, 86]. However, the improved FD model presented in this paper provides a highly accurate, computationally efficient model which can be employed robustly across the parameter space in order to face the challenges of gravitational wave astronomy with current generation ground-based detectors.

VI. ACKNOWLEDGEMENTS

The authors would like to thank Hector Estelles, Jannik Mielke, Lorenzo Pompili, Shaun Swain and Thibaut Wouters for their efforts during the IMRPhenomXPNR code review. Additionally, we would like to thank Edward Fauchon-Jones for his contribution to the production of the BAM NR simulations

displayed in Fig. 1.

EH, MC, AH, JV, FARV and SH were supported by the Universitat de les Illes Balears (UIB); the Spanish Agencia Estatal de Investigación grants PID2022-138626NB-I00, RED2022-134204-E, RED2022-134411-T, funded by MCIN/AEI/10.13039/501100011033 and the ERDF/EU; Comunitat Autònoma de les Illes Balears through the Conselleria d'Educació i Universitats with funds from the European Union - NextGenerationEU/PRTR-C17.I1 (SINCO2022/6719) and from the European Union - European Regional Development Fund (ERDF) (SINCO2022/18146).

JT acknowledges support from the NASA LISA Preparatory Science grant 20-LPS20-0005. CH thanks the UKRI Future Leaders Fellowship for support through the grant MR/T01881X/1. AH is further supported by grant PD-034-2023 co-financed by the Govern Balear and the European Social Fund Plus (ESF+) 2021-2027. JV is additionally supported by the Spanish Ministry of Universities Grant No. FPU22/02211. FARV is also supported through the Conselleria d'Educació i Universitats via an FPI-CAIB doctoral grant (FPI_092_2022). CGQ is supported by the Swiss National Science Foundation (SNSF) Ambizione grant PZ00P2_223711. SG was supported by the Max Planck Society's Independent Research Group program. LL acknowledges support at King's College London from the Royal Society URF\R1\211451. MH was supported by Science and Technology Facilities Council (STFC) grant ST/V00154X/1.

The catalogue of numerical simulations against which this model was calibrated, in addition to the simulations used for comparison in Fig. 1, were performed on the DiRAC@Durham facility, managed by the Institute for Computational Cosmology on behalf of the STFC DiRAC HPC Facility (www.dirac.ac.uk). The equipment was funded by BEIS capital funding via STFC capital grants ST/P002293/1 and ST/R002371/1, Durham University and STFC operations grant ST/R000832/1. In addition, several of the simulations used in the calibration were performed as part of an allocation graciously provided by Oracle to explore the use of our code on the Oracle Cloud Infrastructure.

The authors are additionally grateful for computational resources provided by the LIGO laboratory and supported by National Science Foundation Grants PHY-0757058 and PHY-0823459, which were used to perform the match comparisons presented in this paper.

Parameter estimation and mismatch analyses were performed on a range of computing clusters. These include

the Sciama High Performance Compute (HPC) cluster, which is supported by the ICG, SEPNet and the University of Portsmouth; the Picasso Supercomputer, with technical expertise and assistance provided by the SCBI (Supercomputing and Bioinformatics) center of the University of Malaga supported by grants AECT-2024-2-0017 and AECT-2025-1-0024; MareNostrum 5 at the Barcelona Supercomputing Center supported by grant AECT-2024-3-0027; the DiRAC Data Intensive service (DIAL) at the University of Leicester, managed by the University of Leicester Research Computing Service on behalf of the STFC DiRAC HPC Facility (www.dirac.ac.uk). The DiRAC service at Leicester was funded by BEIS, UKRI and STFC capital funding and STFC operations grants. DiRAC is part of the UKRI Digital Research Infrastructure.

Further analyses were performed on the supercomputing facilities at Cardiff University operated by Advanced Research Computing at Cardiff (ARCCA) on behalf of the Cardiff Supercomputing Facility and the HPC Wales and Supercomputing Wales (SCW) projects. We acknowledge the support of the latter, which is part-funded by the European Regional Development Fund (ERDF) via the Welsh Government. In part the computational resources at Cardiff University were also supported by STFC grant ST/I006285/1.

This research has made use of data or software obtained from the Gravitational Wave Open Science Center (gwosc.org), a service of the LIGO Scientific Collaboration, the Virgo Collaboration, and KAGRA. This material is based upon work supported by NSF's LIGO Laboratory which is a major facility fully funded by the National Science Foundation, as well as the Science and Technology Facilities Council (STFC) of the United Kingdom, the Max-Planck-Society (MPS), and the State of Niedersachsen/Germany for support of the construction of Advanced LIGO and construction and operation of the GEO600 detector. Additional support for Advanced LIGO was provided by the Australian Research Council. Virgo is funded, through the European Gravitational Observatory (EGO), by the French Centre National de Recherche Scientifique (CNRS), the Italian Istituto Nazionale di Fisica Nucleare (INFN) and the Dutch Nikhef, with contributions by institutions from Belgium, Germany, Greece, Hungary, Ireland, Japan, Monaco, Poland, Portugal, Spain. KAGRA is supported by Ministry of Education, Culture, Sports, Science and Technology (MEXT), Japan Society for the Promotion of Science (JSPS) in Japan; National Research Foundation (NRF) and Ministry of Science and ICT (MSIT) in Korea; Academia Sinica (AS) and National Science and Technology Council (NSTC) in Taiwan.

-
- [1] R. Abbott *et al.* (LIGO Scientific, Virgo, KAGRA), *Phys. Rev. X* **13**, 041039 (2023), [arXiv:2111.03606 \[gr-qc\]](https://arxiv.org/abs/2111.03606).
 - [2] R. Abbott, T. Abbott, K. Ackley, C. Adams, V. Adya, C. Affeldt, M. Agathos, *et al.*, *Living reviews in relativity* **23**, 1 (2020).
 - [3] M. Punturo *et al.*, *Class. Quant. Grav.* **27**, 084007 (2010).
 - [4] S. Hild *et al.*, *Class. Quant. Grav.* **28**, 094013 (2011), [arXiv:1012.0908 \[gr-qc\]](https://arxiv.org/abs/1012.0908).
 - [5] B. P. Abbott *et al.* (LIGO Scientific), *Class. Quant. Grav.* **34**, 044001 (2017), [arXiv:1607.08697 \[astro-ph.IM\]](https://arxiv.org/abs/1607.08697).
 - [6] D. Reitze *et al.*, *Bull. Am. Astron. Soc.* **51**, 035 (2019), [arXiv:1907.04833 \[astro-ph.IM\]](https://arxiv.org/abs/1907.04833).
 - [7] T. A. Apostolatos, C. Cutler, G. J. Sussman, and K. S. Thorne, *Phys. Rev. D* **49**, 6274 (1994).
 - [8] L. E. Kidder, *Phys. Rev. D* **52**, 821 (1995), [arXiv:gr-qc/9506022](https://arxiv.org/abs/gr-qc/9506022).
 - [9] B. P. Abbott *et al.* (LIGO Scientific, Virgo), *Phys. Rev. Lett.* **116**, 061102 (2016), [arXiv:1602.03837 \[gr-qc\]](https://arxiv.org/abs/1602.03837).
 - [10] B. P. Abbott *et al.* (LIGO Scientific, Virgo), *Phys. Rev. Lett.* **116**, 241102 (2016), [arXiv:1602.03840 \[gr-qc\]](https://arxiv.org/abs/1602.03840).
 - [11] P. Schmidt, M. Hannam, S. Husa, and P. Ajith, *Phys. Rev. D* **84**, 024046 (2011), [arXiv:1012.2879 \[gr-qc\]](https://arxiv.org/abs/1012.2879).
 - [12] P. Schmidt, M. Hannam, and S. Husa, *Phys. Rev. D* **86**, 104063 (2012), [arXiv:1207.3088 \[gr-qc\]](https://arxiv.org/abs/1207.3088).
 - [13] R. O'Shaughnessy, B. Vaishnav, J. Healy, Z. Meeks, and D. Shoemaker, *Phys. Rev. D* **84**, 124002 (2011), [arXiv:1109.5224 \[gr-qc\]](https://arxiv.org/abs/1109.5224).
 - [14] M. Boyle, R. Owen, and H. P. Pfeiffer, *Phys. Rev. D* **84**, 124011 (2011), [arXiv:1110.2965 \[gr-qc\]](https://arxiv.org/abs/1110.2965).
 - [15] G. Pratten, S. Husa, C. Garcia-Quiros, M. Colleoni, A. Ramos-

- Buades, H. Estelles, and R. Jaume, *Phys. Rev. D* **102**, 064001 (2020), [arXiv:2001.11412 \[gr-qc\]](#).
- [16] M. Colleoni, F. A. Ramis Vidal, C. García-Quirós, S. Akçay, and S. Bera, *Phys. Rev. D* **111**, 104019 (2025).
- [17] H. Estellés, M. Colleoni, C. García-Quirós, S. Husa, D. Keitel, M. Mateu-Lucena, M. d. L. Planas, and A. Ramos-Buades, *Phys. Rev. D* **105**, 084040 (2022), [arXiv:2105.05872 \[gr-qc\]](#).
- [18] A. Ramos-Buades, A. Buonanno, H. Estellés, M. Khalil, D. P. Mihaylov, S. Ossokine, L. Pompili, and M. Shiferaw, *Phys. Rev. D* **108**, 124037 (2023), [arXiv:2303.18046 \[gr-qc\]](#).
- [19] R. Gamba, D. Chiaramello, and S. Neogi, *Phys. Rev. D* **110**, 024031 (2024), [arXiv:2404.15408 \[gr-qc\]](#).
- [20] C. García-Quirós, M. Colleoni, S. Husa, H. Estellés, G. Pratten, A. Ramos-Buades, M. Mateu-Lucena, and R. Jaume, *Phys. Rev. D* **102**, 064002 (2020), [arXiv:2001.10914 \[gr-qc\]](#).
- [21] G. Pratten *et al.*, *Phys. Rev. D* **103**, 104056 (2021), [arXiv:2004.06503 \[gr-qc\]](#).
- [22] J. E. Thompson, E. Hamilton, L. London, S. Ghosh, P. Kolitsidou, C. Hoy, and M. Hannam, *Phys. Rev. D* **109**, 063012 (2024), [arXiv:2312.10025 \[gr-qc\]](#).
- [23] M. Khalil, A. Buonanno, H. Estelles, D. P. Mihaylov, S. Ossokine, L. Pompili, and A. Ramos-Buades, *Phys. Rev. D* **108**, 124036 (2023), [arXiv:2303.18143 \[gr-qc\]](#).
- [24] L. Pompili *et al.*, *Phys. Rev. D* **108**, 124035 (2023), [arXiv:2303.18039 \[gr-qc\]](#).
- [25] M. van de Meent, A. Buonanno, D. P. Mihaylov, S. Ossokine, L. Pompili, N. Warburton, A. Pound, B. Wardell, L. Durkan, and J. Miller, *Phys. Rev. D* **108**, 124038 (2023), [arXiv:2303.18026 \[gr-qc\]](#).
- [26] D. P. Mihaylov, S. Ossokine, A. Buonanno, H. Estelles, L. Pompili, M. Pürrer, and A. Ramos-Buades, (2023), [arXiv:2303.18203 \[gr-qc\]](#).
- [27] V. Varma, S. E. Field, M. A. Scheel, J. Blackman, L. E. Kidder, and H. P. Pfeiffer, *Phys. Rev. D* **99**, 064045 (2019), [arXiv:1812.07865 \[gr-qc\]](#).
- [28] V. Varma, S. E. Field, M. A. Scheel, J. Blackman, D. Gerosa, L. C. Stein, L. E. Kidder, and H. P. Pfeiffer, *Phys. Rev. Research* **1**, 033015 (2019), [arXiv:1905.09300 \[gr-qc\]](#).
- [29] J. Yoo, V. Varma, M. Giesler, M. A. Scheel, C.-J. Haster, H. P. Pfeiffer, L. E. Kidder, and M. Boyle, *Phys. Rev. D* **106**, 044001 (2022), [arXiv:2203.10109 \[gr-qc\]](#).
- [30] P. Whittle, *Journal of the Royal Statistical Society: Series B (Methodological)* **15**, 125 (2018), https://academic.oup.com/jrsssb/article-pdf/15/1/125/49093751/jrsssb_15_1_125.pdf.
- [31] E. Thrane and C. Talbot, *Publications of the Astronomical Society of Australia* **36** (2019), 10.1017/pasa.2019.2.
- [32] R. Abbott *et al.* (KAGRA, VIRGO, LIGO Scientific), *Phys. Rev. X* **13**, 041039 (2023), [arXiv:2111.03606 \[gr-qc\]](#).
- [33] K. Chatziioannou, A. Klein, N. Cornish, and N. Yunes, *Phys. Rev. Lett.* **118**, 051101 (2017), [arXiv:1606.03117 \[gr-qc\]](#).
- [34] K. Chatziioannou, A. Klein, N. Yunes, and N. Cornish, *Phys. Rev. D* **95**, 104004 (2017), [arXiv:1703.03967 \[gr-qc\]](#).
- [35] E. Hamilton, L. London, J. E. Thompson, E. Fauchon-Jones, M. Hannam, C. Kalaghatgi, S. Khan, F. Pannarale, and A. Vano-Vinuales, *Phys. Rev. D* **104**, 124027 (2021), [arXiv:2107.08876 \[gr-qc\]](#).
- [36] S. Ghosh, P. Kolitsidou, and M. Hannam, *Phys. Rev. D* **109**, 024061 (2024), [arXiv:2310.16980 \[gr-qc\]](#).
- [37] P. Ajith, M. Hannam, S. Husa, Y. Chen, B. Brügmann, N. Dorband, D. Müller, F. Ohme, D. Pollney, C. Reisswig, L. Santamaría, and J. Seiler, *Phys. Rev. Lett.* **106**, 241101 (2011).
- [38] P. Schmidt, F. Ohme, and M. Hannam, *Phys. Rev. D* **91**, 024043 (2015).
- [39] E. Hamilton *et al.*, *Phys. Rev. D* **109**, 044032 (2024), [arXiv:2303.05419 \[gr-qc\]](#).
- [40] E. Hamilton, L. London, and M. Hannam, (2023), [arXiv:2301.06558 \[gr-qc\]](#).
- [41] B. Bruegmann, J. A. Gonzalez, M. Hannam, S. Husa, and U. Sperhake, *Phys. Rev. D* **77**, 124047 (2008), [arXiv:0707.0135 \[gr-qc\]](#).
- [42] M. Boyle, L. E. Kidder, S. Ossokine, and H. P. Pfeiffer, (2014), [arXiv:1409.4431 \[gr-qc\]](#).
- [43] C. Kalaghatgi and M. Hannam, *Phys. Rev. D* **103**, 024024 (2021), [arXiv:2008.09957 \[gr-qc\]](#).
- [44] H. Estellés, A. Buonanno, R. Enficiaud, C. Foo, and L. Pompili, “Adding equatorial-asymmetric effects for spin-precessing binaries into the SEOBNRv5PHM waveform model,” (2025), in preparation.
- [45] J. Mielke, S. Ghosh, A. Borchers, and F. Ohme, *Phys. Rev. D* **111**, 064009 (2025), [arXiv:2412.06913 \[gr-qc\]](#).
- [46] X. Jiménez-Forteza, D. Keitel, S. Husa, M. Hannam, S. Khan, and M. Pürrer, *Phys. Rev. D* **95**, 064024 (2017), [arXiv:1611.00332 \[gr-qc\]](#).
- [47] M. Boyle *et al.*, *Class. Quant. Grav.* **36**, 195006 (2019), [arXiv:1904.04831 \[gr-qc\]](#).
- [48] S. Khan, K. Chatziioannou, M. Hannam, and F. Ohme, *Phys. Rev. D* **100**, 024059 (2019), [arXiv:1809.10113 \[gr-qc\]](#).
- [49] LSC, “Updated Advanced LIGO sensitivity design curve,” <https://dcc.ligo.org/LIGO-T1800044/public>, LIGO Document T1800044-v5.
- [50] R. Abbott *et al.* (LIGO Scientific, Virgo), *Phys. Rev. Lett.* **125**, 101102 (2020), [arXiv:2009.01075 \[gr-qc\]](#).
- [51] E. Baird, S. Fairhurst, M. Hannam, and P. Murphy, *Phys. Rev. D* **87**, 024035 (2013), [arXiv:1211.0546 \[gr-qc\]](#).
- [52] J. Skilling, *Bayesian Anal.* **1**, 833 (2006).
- [53] J. S. Speagle, *Monthly Notices of the Royal Astronomical Society* **493**, 3132?3158 (2020).
- [54] G. Ashton *et al.*, *Astrophys. J. Suppl.* **241**, 27 (2019), [arXiv:1811.02042 \[astro-ph.IM\]](#).
- [55] I. M. Romero-Shaw *et al.*, *Mon. Not. Roy. Astron. Soc.* **499**, 3295 (2020), [arXiv:2006.00714 \[astro-ph.IM\]](#).
- [56] R. Abbott *et al.* (KAGRA, VIRGO, LIGO Scientific), *Astrophys. J. Suppl.* **267**, 29 (2023), [arXiv:2302.03676 \[gr-qc\]](#).
- [57] J. Aasi *et al.* (LIGO Scientific), *Class. Quant. Grav.* **32**, 074001 (2015), [arXiv:1411.4547 \[gr-qc\]](#).
- [58] F. Acernese *et al.* (VIRGO), *Class. Quant. Grav.* **32**, 024001 (2015), [arXiv:1408.3978 \[gr-qc\]](#).
- [59] LIGO Scientific Collaboration and Virgo Collaboration, “Noise curves used for simulations in the update of the observing scenarios paper,” DCC (2022).
- [60] C. Hoy, S. Akçay, J. Mac Uilliam, and J. E. Thompson, (2024), [arXiv:2409.19404 \[gr-qc\]](#).
- [61] R. Abbott *et al.* (KAGRA, VIRGO, LIGO Scientific), *Phys. Rev. X* **13**, 011048 (2023), [arXiv:2111.03634 \[astro-ph.HE\]](#).
- [62] T. D. Abbott *et al.* (LIGO Scientific, Virgo), *Phys. Rev. X* **6**, 041014 (2016), [arXiv:1606.01210 \[gr-qc\]](#).
- [63] S. M. Gaebel and J. Veitch, *Class. Quant. Grav.* **34**, 174003 (2017), [arXiv:1703.08988 \[astro-ph.IM\]](#).
- [64] J. E. Thompson, C. Hoy, E. Fauchon-Jones, and M. Hannam, (2025), [arXiv:2506.10530 \[gr-qc\]](#).
- [65] R. Abbott *et al.* (LIGO Scientific, Virgo), *Phys. Rev. D* **102**, 043015 (2020), [arXiv:2004.08342 \[astro-ph.HE\]](#).
- [66] C. Hoy, C. Mills, and S. Fairhurst, *Phys. Rev. D* **106**, 023019 (2022), [arXiv:2111.10455 \[gr-qc\]](#).
- [67] C. Hoy, S. Fairhurst, and I. Mandel, *Phys. Rev. D* **111**, 023037 (2025), [arXiv:2408.03410 \[gr-qc\]](#).
- [68] T. Islam, S. E. Field, C.-J. Haster, and R. Smith, *Phys. Rev. D* **103**, 104027 (2021), [arXiv:2010.04848 \[gr-qc\]](#).
- [69] M. Hannam *et al.*, *Nature* **610**, 652 (2022), [arXiv:2112.11300 \[gr-qc\]](#).
- [70] E. Payne, S. Hourihane, J. Golomb, R. Udall, R. Udall, D. Davis, and K. Chatziioannou, *Phys. Rev. D* **106**, 104017 (2022), [arXiv:2206.11932 \[gr-qc\]](#).
- [71] R. Macas, A. Lundgren, and G. Ashton, *Phys. Rev. D* **109**, 062006 (2024), [arXiv:2311.09921 \[gr-qc\]](#).

- [72] I. M. Romero-Shaw, P. D. Lasky, and E. Thrane, *Astrophys. J.* **940**, 171 (2022), [arXiv:2206.14695 \[astro-ph.HE\]](#).
- [73] N. Gupte *et al.*, (2024), [arXiv:2404.14286 \[gr-qc\]](#).
- [74] M. d. L. Planas, A. Ramos-Buades, C. García-Quirós, H. Estellés, S. Husa, and M. Haney, (2025), [arXiv:2504.15833 \[gr-qc\]](#).
- [75] S. Ossokine *et al.*, *Phys. Rev. D* **102**, 044055 (2020), [arXiv:2004.09442 \[gr-qc\]](#).
- [76] M. Colleoni, M. Mateu-Lucena, H. Estellés, C. García-Quirós, D. Keitel, G. Pratten, A. Ramos-Buades, and S. Husa, *Phys. Rev. D* **103**, 024029 (2021), [arXiv:2010.05830 \[gr-qc\]](#).
- [77] P. Kolitsidou, J. E. Thompson, and M. Hannam, *Phys. Rev. D* **111**, 024050 (2025), [arXiv:2402.00813 \[gr-qc\]](#).
- [78] H. Qi and V. Raymond, *Phys. Rev. D* **104**, 063031 (2021), [arXiv:2009.13812 \[gr-qc\]](#).
- [79] S. Morisaki, R. Smith, L. Tsukada, S. Sachdev, S. Stevenson, C. Talbot, and A. Zimmerman, *Phys. Rev. D* **108**, 123040 (2023), [arXiv:2307.13380 \[gr-qc\]](#).
- [80] S. Morisaki, *Phys. Rev. D* **104**, 044062 (2021), [arXiv:2104.07813 \[gr-qc\]](#).
- [81] M. d. L. Planas, J. Llobera-Querol, and S. Husa, *Phys. Rev. D* **109**, 124028 (2024), [arXiv:2401.13342 \[gr-qc\]](#).
- [82] A. Elhashash and D. A. Nichols, (2025), [arXiv:2504.18635 \[gr-qc\]](#).
- [83] M. Rosselló-Sastre, S. Husa, and S. Bera, *Phys. Rev. D* **110**, 084074 (2024), [arXiv:2405.17302 \[gr-qc\]](#).
- [84] S. Albanesi, R. Gamba, S. Bernuzzi, J. Fontbuté, A. Gonzalez, and A. Nagar, (2025), [arXiv:2503.14580 \[gr-qc\]](#).
- [85] M. L. Katz, J.-B. Bayle, A. J. K. Chua, and M. Vallisneri, *Phys. Rev. D* **106**, 103001 (2022), [arXiv:2204.06633 \[gr-qc\]](#).
- [86] J. Valencia and S. Husa, (2025), [arXiv:2505.09600 \[gr-qc\]](#).